CASES-97: LATE-MORNING WARMING AND MOISTENING OF THE CONVECTIVE BOUNDARY LAYER OVER THE WALNUT RIVER WATERSHED

MARGARET A. LEMONE*
National Center for Atmospheric Research, Boulder, Colorado, 80307, U.S.A.

ROBERT L. GROSSMAN
PAOS, University of Colorado, Boulder, Colorado, U.S.A.

ROBERT T. MCMILLEN
NOAA Atmospheric Turbulence and Diffusion Division, Oak Ridge, Tennessee, U.S.A.

KUO-NAN LIOU and S.C. OU
Department of Atmospheric Science, UCLA, Los Angeles, California U.S.A.

STUART MCKEEN and WAYNE ANGEVINE
CIRES, University of Colorado and NOAA Aeronomy Laboratory, Boulder, Colorado, U.S.A.

KYOKO IKEDA and FEI CHEN
National Center for Atmospheric Research, Boulder, Colorado, 80307, U.S.A.

(Received in final form 29 October 2001)

Abstract. Aircraft, radiosonde, surface-flux, and boundary-layer wind profiler data from the Cooperative Atmosphere Surface Exchange Study's 1997 field project, CASES-97, are combined with synoptic data to study the evolution of the vertically-averaged mixed-layer potential temperature $[\Theta]$ and mixing-ratio $[Q]$ on three nearly-cloudless days from 1000 CST to 1200 CST (local noon is approximately 1230 CST). This was achieved through examination of the terms in the time-tendency ('budget') equations for $[\Theta]$ and $[Q]$. We estimate three of the terms – local time rate of change, vertical flux divergence, and horizontal advection. For the $[Q]$-budget, vertical flux divergence usually dominates, but horizontal advection is significant on one of the three days. The $[Q]$-budget balances for two of the three days to within the large experimental error. For the Θ-budget, vertical flux divergence accounts for most of the morning warming, with horizontal advection of secondary importance. The residual in the Θ-budget has the same sign for all three days, indicating that not all the heating is accounted for. We can balance the $[\Theta]$-budgets to within experimental error on two of the three days by correcting the vertical-flux divergence for apparent low biases in the flux measurements of one of the aircraft and in the surface fluxes, and accounting for direct heating of the mixed layer by radiative flux divergence allowing for the effects of carbonaceous aerosols. The $[\Theta]$-budget with these corrections also balances on the third day if horizontal gradients from synoptic maps are used to estimate the horizontal advection. However, the corrected budget for this day does not balance if the horizontal gradient in the advection term is estimated using CASES-97 aircraft and radiosondes; we suggest that persistent mesoscale circulations led to an overestimate of the horizontal gradient and hence horizontal advection.

Keywords: Convective boundary layer, Diurnal cycle, Mixed layer, Radiative heating, Surface-mixed layer interaction, Vegetation and soil moisture effects.

* E-mail: lemone@ucar.edu.us

Boundary-Layer Meteorology **104:** 1–52, 2002.

1. Introduction

Data from the 21 April–21 May 1997 fair-weather portion of the Cooperative Atmosphere-Surface Exchange Study (CASES-97, LeMone et al., 2000) field project are used to determine the processes warming and moistening the atmospheric mixed layer between 1000 and 1200 CST (local noon is approximately 1230 CST) over a watershed with heterogeneous surface cover and 150-m terrain variation. We will look at three fair-weather days with no low clouds, but with different surface characteristics and synoptic situations. 1000 CST is late enough so that surface heterogeneities in temperature and mixing ratio that developed during the night have mostly disappeared, but early enough so that there is significant time evolution. We define the mixed layer as the layer over which horizontally-averaged potential temperature is approximately constant with height. This study represents a part of a longer-term effort to characterise, explain, and parameterise the behaviour of the fair weather planetary boundary layer over land, as a function of surface characteristics and the synoptic situation, during the entire diurnal cycle.

The data were collected in the Atmospheric Boundary Layer Experiments (ABLE) array (Coulter et al., 1998; LeMone et al., 2000) between 21 April and 21 May 1997. Operated by Argonne National Laboratory, ABLE occupies the southern two-thirds of the Walnut River Watershed in south-central Kansas, just east of Wichita, in the central United States. The terrain varies in elevation from about 480 m above sea level at the edges of the watershed to around 360 m at its mouth (Figure 1). The surface cover is mostly grassland (pasture) to the east of the Walnut River, and mostly crops (mainly winter wheat) with more settlement to the west of the river. The grass was dormant and the winter wheat was growing rapidly during the beginning of CASES-97, but all of the vegetation was green by the end. Five rainfall events during the field program combined with differing synoptics and vegetative cover to provide a variety of situations for study.

We look at the physical processes changing potential temperature θ and mixing ratio q through examining their budget equations. We represent θ or q by the variable $\psi = \Psi + \psi'$, where, Ψ (upper case) is the horizontal average, or 'large' scale, and ψ' represents fluctuations on smaller scales. Averaging horizontally such that the 'mixed' terms are zero (e.g., $\partial \overline{w'\Psi}/\partial z$, where the overbar denotes the 'large-scale' average), we obtain the relationship:

$$\frac{\partial \Psi}{\partial t} + \frac{\partial}{\partial z}\overline{w'\psi'} + \vec{V}_h \cdot \nabla \Psi + S \approx 0, \tag{1a}$$

where $\vec{V}_h$ is the large-scale horizontal wind vector and S represents sources of Ψ. Horizontal turbulence flux divergence and vertical advection by large-scale subsidence are assumed small and have been neglected. In practice, the average is in time and space, so care is taken to isolate diurnal changes from the vertical and horizontal gradients. Since there was no low cloud during the times of interest on the days analysed, the source term S is equal to the radiative flux divergence

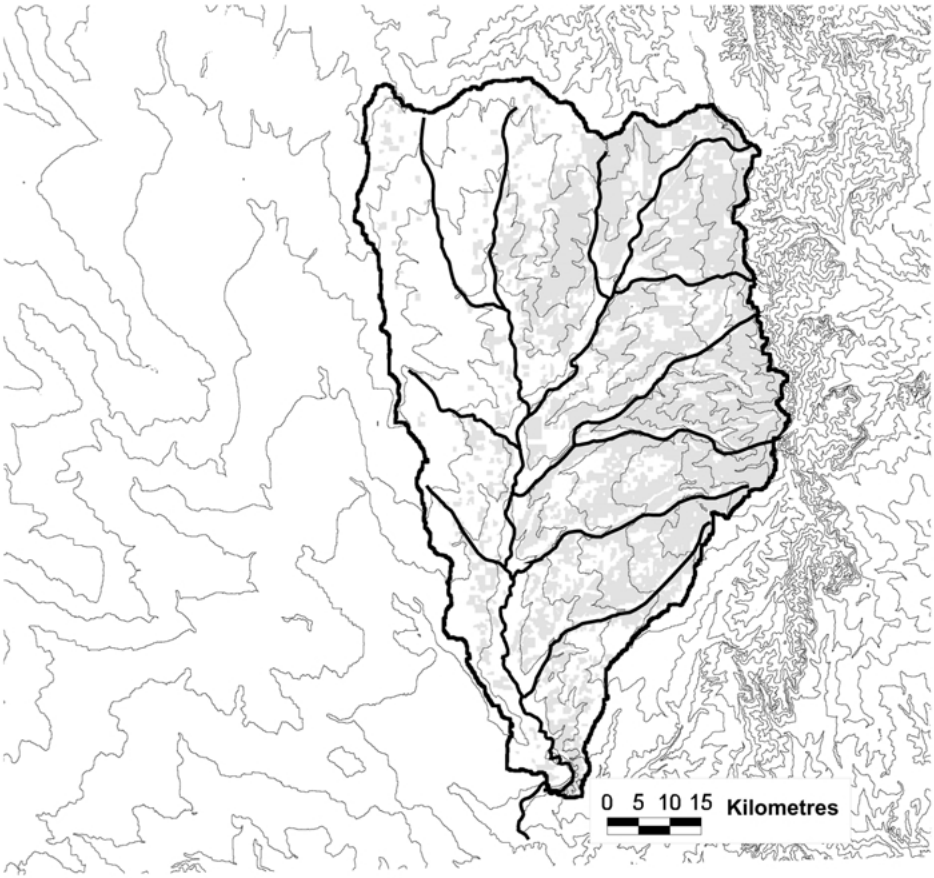

Figure 1. Topography, major streams, and idealized land use map for the Walnut River watershed, where CASES-97 took place. Shading indicates pasture. Crops (mainly winter wheat) and settlements are concentrated to the west of the Walnut River, which runs north-south. From LeMone et al. (2000), with permission from the American Meteorological Society. Contour interval is 20 m.

$\partial F_r/\partial z$ for the Θ-budget, and is zero for the Q-budget. Thus the terms are, from left to right, the time-tendency term, the vertical flux divergence term, the large-scale horizontal advection term, and the source term.

Averaging vertically through the mixed layer and assuming that $\vec{V}_h$ is constant with height,

$$\left[\frac{\partial \Psi}{\partial t}\right] + \left[\frac{\partial}{\partial z}\overline{w'\psi'}\right] + [\vec{V}_h] \cdot \nabla[\Psi] + [S] \approx 0, \tag{1b}$$

where [ ] denotes a vertical average from about 2 m above the surface to the mixed-layer top h, as defined by the top of the constant-Θ layer, where typically the mixing ratio Q starts to decrease significantly.

Budgets of Θ and Q have been computed previously by several authors. The First ISLSCP Field Experiment (FIFE, Sellers et al., 1992) led to several budget studies using a combination of aircraft, radiosonde, and surface data collected from as early as 0800 LST* to as late as 1620 LST (Betts et al., 1990; Betts, 1992; Grossman, 1992). Those budget studies relying on vertical divergences of aircraft-derived fluxes typically could not account for up to about half of the morning heating (e.g., Betts et al., 1990; Grossman, 1992). The discrepancies were attributed to aircraft underestimates of heat fluxes in the lower boundary layer, a conclusion based on extrapolation of aircraft profiles to surface-based heat flux estimates; or to horizontal advection, which was difficult to measure over the small (15 km $\times$ 15 km) FIFE domain (Betts et al., 1990; Grossman, 1992). Mixing-ratio budgets had comparable or larger errors, but no systematic pattern was observed. Afternoon budgets tended to balance to within measurement error. Other budgets have been computed with fewer measurement platforms. Barr and Betts (1997) used radiosonde observations to estimate mixed-layer and entrainment-layer budgets for the Boreal Ecosystem-Atmospheric Study (BOREAS, Sellers et al., 1995), with advection from synoptic analyses. Furger et al. (1995) discussed budgets from wind-profiler networks with Radio-Acoustic Sounding Systems (RASS).

Direct heating or cooling of the boundary layer by radiative processes was neglected in these studies or estimated to be small. However, several situations have been identified in which radiative flux divergence is important to the heating or cooling of the boundary layer. Nicholls et al. (1982) found that the sum of the vertical flux divergence (warming), horizontal advection (warming), and radiative terms (cooling) balanced the observed warming in a fair-weather boundary layer over the eastern tropical Atlantic Ocean, documented during the Global Atmospheric Research Program's Atlantic Tropical Experiment (GATE). Parsons et al. (2000) used data from dry-air intrusions collected during TOGA COARE** to demonstrate that radiative flux divergence can have a significant effect on the strength of the inversion at the top of the atmospheric mixed layer over the tropical Pacific ocean. Satheesh and Ramanathan (2000) documented direct heating of the atmosphere over the tropical Indian Ocean by mainly soot aerosols transported off the Asian continent by the winter monsoon. For the boundary layer over land, Angevine et al. (1998b) and Angevine (1999) concluded that direct heating through absorption of shortwave radiation by aerosols contributed about 0.1 K hr^{-1} to warming For comparison, we observe mid-morning Θ increases of the order of 0.7 to 1.3 K hr^{-1}.

The CASES-97 dataset is sufficiently comprehensive that there is potential to evaluate thermodynamic budgets more accurately than previously. Aircraft, radar wind profilers, radiosondes, and surface data provide cross-checks of winds, gradi-

* Local standard time is used here since it is tied to boundary-layer development.

** Tropical Ocean Global Atmosphere Coupled Ocean-Atmosphere Response Experiment.

ents, and time changes, over a domain 60 km across – four times the width of the FIFE domain. Mixed-layer depth is based on profilers, radiosondes, and aircraft soundings. Time tendency is found from aircraft data and radiosondes. Vertical flux divergences are based on data from aircraft and surface flux towers; and $\partial\overline{w'q'}/\partial z$ is also estimated by differencing surface fluxes and $\overline{w'q'}$ at boundary-layer top z_i, found from $\overline{w'\theta'}|_{zi}$ and differences in Θ and Q across z_i, as described in Betts et al. (1992) and Betts (1992). For horizontal advection, winds are based on aircraft and profilers, and horizontal gradients on aircraft, radiosondes, and Eta model products. We find that the vertical flux divergence is important in both budgets, and horizontal advection can be significant for the $[Q]$-budget. Even after great care in estimating these terms, there is a systematic imbalance in the $[\Theta]$-budget: not all the warming is accounted for. We provide evidence that the imbalance is related to (a) a low bias in θ flux for one of the aircraft; (b) a low bias in surface fluxes; (c) neglect of direct radiative heating of the mixed layer; and on one day; (d) the influence of mesoscale (10–100 km) structure on the estimate of horizontal advection. The $[Q]$-budgets balance to within the large uncertainty of the terms for two of the three days.

The instrumentation and basic analysis are discussed in Section 2. Section 3 describes the days selected, as background for both computations and discussion of budgets. Section 4 describes the budget calculations and estimates of uncertainties. The budgets and imbalance are discussed in Section 5. Section 6 summarises the results.

2. Experimental Strategy, Platforms, and Instruments

2.1. CASES-97

The CASES-97 experimental array appears in Figure 2. BEA (Beaumont), WHI (Whitewater) and OXF (Oxford) are ABLE wind profiling systems equipped with RASS. The profiling systems sampled winds using 915-MHz Doppler radar wind profilers, Doppler minisodars, and at Beaumont and Oxford, automated weather stations. The numbered squares in Figure 2 denote flux stations, sited at a range of elevations and in rough proportion to land cover. Here, we use basic meteorological measurements (wind, temperature, specific humidity, pressure) and eddy-correlation heat and moisture fluxes from sites 1–8 (operated by NCAR) and site 10 (operated by the NOAA Atmospheric Turbulence and Diffusion Division (ATDD)).

Additional measurements were taken during the six Intensive Observing Periods (IOPs, Table I), which coincided with typically 24-hour periods of fair weather with nearly clear skies and little evolution in the synoptic pressure field. NCAR CLASS* radiosondes were released every 90 minutes from the three profiler sites.

* Cross-Chain LORAN Sounding System.

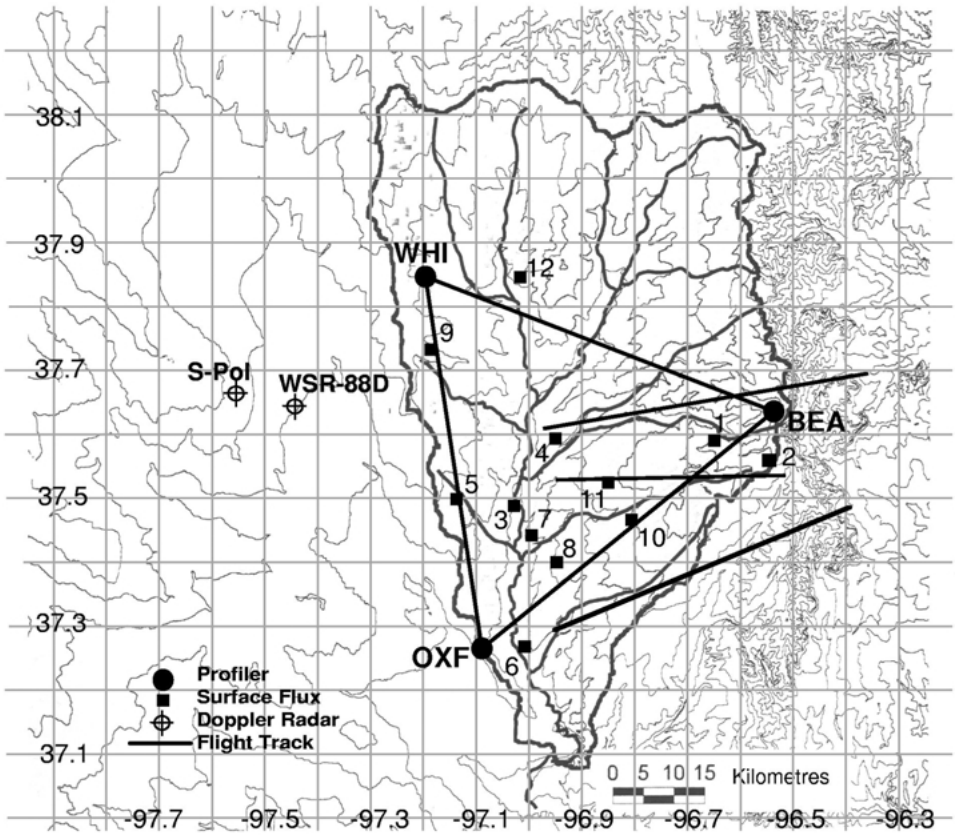

Figure 2. The instrumentation and preset flight tracks for CASES-97. Numbered sites are surface stations that provided eddy-correlation fluxes as well as meteorological data; stations 1–8 and 10 were used. Stations 1–6 are NCAR Portable Automated Mesonet (PAM) IIIs (Horst and Oncley 1995, Millitzer et al. 1995), stations 7 and 8 are NCAR ASTER (Atmosphere-Surface Turbulent Exchange Research) sites; station 10 was operated by NOAA Atmospheric Turbulence and Diffusion Division. BEA, OXF, and WHI are ABLE profiling sites with collocated NCAR/CLASS radiosonde systems. Automated weather stations (AWSs) were located at OXF, BEA, and site 11. S-Pol is the NCAR S-band polarimetric Doppler radar. Contour interval is 20 m; radar wind profiling site elevations (m msl) are: Beaumont, 478; Oxford, 360; Whitewater, 420. Adapted from Figure 7 of LeMone et al. (2000), with permission from the American Meteorological Society.

Additionally, the NOAA Twin Otter and University of Wyoming King Air flew two coordinated flight patterns, one in the morning and one in the afternoon, to coincide with times of more rapid evolution. During each pattern, the two aircraft sampled vertical flux profiles, horizontal fields, and mixed-layer depth h by alternating straight and level flight legs (flux legs) at two or more altitudes with soundings through h. Because of the difference in typical true air speeds, the King Air typically flew 'stack patterns', which consisted of 4–5 flux legs from about 30 m above ground level (agl) to just below the inversion; while the Twin Otter

typically flew 'cat's-ears' patterns, which alternated flux legs at about 30 m agl and just below the inversion with soundings through h at the ends of the upper leg. The morning flux pattern consisted of about four stacks and five cat's-ears patterns and lasted from about 0830 to 1230 CST. At the end of the flux pattern, one aircraft flew straight and level legs around the perimeter of the array within the mixed layer ('triangle patterns' or 'triangles'). Pre-set locations of the triangle and flux pattern tracks appear in Figure 2. Toward the end of the experiment, an east-west track was flown across station 10, and north-south tracks were sometimes flown near the top of the mixed layer. Often the two aircraft landed for refueling for the afternoon mission at Augusta Airport, about 11 km north-west of site 4 in Figure 2, to avoid the 30-minute ferry to the aircraft base at Ponca City, Oklahoma.

2.2. DATA AND DATA PROCESSING

2.2.1. *Aircraft (Tendency Term, Flux Term, Advection Term, Mixed-Layer Top)*

Each aircraft has a gust probe system and fast temperature and water-vapor sensors for estimates of heat and moisture fluxes. The Twin Otter instrumentation is similar to that described in Wellman et al. (1996). Its turbulence measurement system is an outgrowth of that described in Crawford and Dobosy (1992), but now relies on Global Position System (GPS) techniques for aircraft velocity, position, elevation, and attitude. Mixing ratio is sampled using an in-house developed InfraRed Gas Analyser (IRGA, Auble and Myers, 1992); temperature is sampled using a Veco #31A401A thermistor in Rosemount housing, and atmospheric pressure using a Rosemount #1201 sensor. Aircraft-relative winds are based on pressure fluctuations sampled at nine locations on a sphere on the aircraft nose, following Brown et al. (1983). On the King Air, temperature measurements are from a modified version of the Friehe Probe (Friehe and Khelif, 1993) and pressure from the Rosemount 1501 probe. Mixing ratio is from a LiCor 6262 gas analyser. The King Air has a Rosemount 858AJ/1332 differential pressure gust-probe system to sample aircraft-relative winds and a Honeywell Laseref SM inertial navigation system to sample aircraft attitude and motions relative to earth. Further detail on the King Air can be found at http://flights.uwyo.edu/base/

Fluxes, mean quantities, and gradients were computed for each flux leg. Leg end points were determined using altitude, heading, and roll. Roll was required to be less than about 5°, but excursions exceeding this value for a few seconds were accepted. Finding an appropriate altitude criterion was less straightforward. With 150 m variation in surface elevation, the practice of flying the lowest legs at constant height above the ground and higher-level legs at constant pressure altitude led to some difficulty in determining leg ends, particularly at the eastern end of the track just north of Beaumont, where the terrain elevation falls off rapidly (Figure 2). We include the leg segment flown east of Beaumont, since eliminating that portion did not significantly affect the fluxes. Using the technique described in Grossman (1977), we found aircraft mean wind biases were negligible. Fluxes were calculated

TABLE I
CASES-97 fair weather Intensive Observing Periods (IOPs).

IOP	Date	Time (CST)	Wind ($m\ s^{-1}$)	Cloud	Time since last rain	IR sfc temp* (°C)	Grass	Winter wheat (height in m)
1	28–29 Apr	1530 28 Apr–1830 29 Apr	S 10**	Broken Ci**	> 7 days	35 ± 4.9**	Dormant	0.30–0.45 (1 May)
2	4–5 May	0500–0330	S 10	Clear	2 days			
3	10–11 May	0500–0330	SSW 5–6	Clear	2 days	33 ± 4.6	Some green	0.6–0.9 (12 May)
4	16 May	0500–2000	S 6–8	Clear	3 days			
5	20–21 May	0500–0330	ENE 6–7	Scattered Ci	1 day	29 ± 2.7	Green	0.6–0.9, maturing (20 May)

* Uncorrected Heiman downward-looking radiometer data from low-level King-Air flight legs.
** Conditions are for 29 April.

after removing linear trends. For the King Air, the temperature signal had to be advanced 0.1 sec and the mixing ratio signal 0.3 sec before computing fluxes, due to differences in instrument response and location on the aircraft.

In (1b), the height coordinate z is relative to the surface. The King Air APN-159 radar altimeter measured z through and above the mixed layer. However, the Twin Otter Sperry RT-220 radar altimeter only measured z to 818 m, so we used GPS altitude to obtain z at higher altitudes. Unfortunately, the GPS altitude had an absolute offset, which varied from flight to flight. Further, a linear fit of radar altitude z_{ralt} vs. GPS altitude z_{GPS} averaged along a common flight track* showed that $\partial z_{GPS}/\partial z_{ralt} \approx 1.07 \pm 0.02$ for the days examined. We concluded that the change in GPS altitude was more accurate, since plots of z_{GPS} against temperature produced an adiabatic lapse rate in the middle-to-upper mixed layer, consistent with radiosonde data. Also, z_{gps} varied consistently with pressure altitudes computed for one of the days.

Thus, the following procedure was adopted for the Twin Otter. For legs with $z_{ralt} < 818$ m agl, the mean leg altitude is computed from $z = 1.07 \times z_{ralt}$, the leg-averaged radar altitude. For legs with $z > 818$ m agl, an additional step is necessary. First, a least-squares linear fit is performed between z_{GPS} and $1.07 z_{ralt}$ for the common flight track for that flux pattern, using legs with $z_{ralt} < 818$ m. If the leg corresponds to the common flight track, z_{GPS} is plugged into the best-fit line equation to obtain z. If the flux leg extends beyond the common flight track, a correction is necessary to allow for differences between the surface elevation beneath the common flight track and the surface elevation beneath the extension. Mixed-layer depth h from aircraft soundings is similarly estimated using the common-flux-leg least-squares relationship and the difference between the surface elevation beneath the common flight track and the surface elevation beneath where the aircraft intercepted h.

2.2.2. *Profilers (Advection Calculation, Inversion Base)*

Data from the three radar wind profilers are available along with documentation over the Internet at http://www.atmos.anl.gov/ABLE. The Beaumont and Whitewater radars alternate 30-s scans in five directions at high power (low vertical resolution) and low power (high vertical resolution) for 49 minutes out of each hour. We use the consensus average,** which combines the low and high power scans, and which is centered at about 35 min past the hour. The Oxford profiler sampled winds for 30 minutes at high power only, resulting in averages at about 22 min past the hour. We interpolate the three radars to 30 min past the hour, and average the resulting winds through the mixed layer. Comparison with tower and

* The common flight track is found by shortening longer legs over a track until the latitudes and longitudes of the leg ends are closely matched (within $\sim 0.01°$).

** Typically, one selects a range of wind values, and tests to see if a certain percentage of the samples falls within that range. If so, the samples are averaged. For further information see http://www.arm.gov/docs/instruments/static/

aircraft data implies an uncertainty in profiler winds of $\approx$1 m s^{-1}, some of which could be due to differences in sampling volume (Martner et al., 1993; Angevine and MacPherson, 1995; Angevine et al., 1998a). Mixed-layer heights found by applying the technique of Coulter and Holdridge (1998) to reflectivity signal-to-noise ratios (SNR) were supplied to us by R. Coulter (personal communication, 1999).

2.2.3. *Radiosondes (Tendency Term, Inversion Base, Horizontal Gradients)*
There are four sources of uncertainty in the radiosonde measurements: random inherent sonde error, launch procedure, spatial variability, and a small dry bias for the humidity sensor (Zipser and Johnson, 1998). Accuracy estimates for well-ventilated sondes in equilibrium with the environment at time of release are 0.2 K for temperature and 2% for relative humidity or up to 0.3 g kg^{-1} for q in CASES-97.* Not all CASES-97 sondes were in equilibrium with the environment when launched. Further, horizontal variability of θ and q is significant in the turbulent mixed layer, so that sonde measurements are potentially not representative of the local average. The combination of these factors raises uncertainties to 0.5 K for temperature and 5% for relative humidity or up to 0.8 g kg^{-1} for CASES-97 (e.g., Betts et al., 1990; Weckwerth et al., 1996).

2.2.4. *Surface Data (Surface Fluxes, Surface Tendency Term)*
We arithmetically average the data from nine surface-flux sites, including 8 NCAR sites (1-8 in Figure 2) and a NOAA site (10), to obtain surface values of latent and sensible heat flux (LE and H), air temperature, and specific humidity. These quantities were all sampled at 2–3 m above the surface. Sites were chosen to represent the main land-use types (grass, winter wheat, bare fields) in proportion to their occurrence. Surface fluxes were calculated at half-hourly intervals using eddy correlation techniques. The NCAR LE and H fluxes are based on sonic-thermo-anemometer and Krypton-hygrometer measurements (Horst and Oncley, 1995; Millitzer et al., 1995).** For the NOAA tower, a combination of the IRGA and a sonic thermo-anemometer was used. Data at the NOAA site were collected from 3 May to 21 May.

Using an approximate form of the energy balance test described in Twine et al. (2000) the average ratio of heat fluxes to net radiation minus soil heating, ($[H + LE]/[R_n - G]$), is 0.91 for 29 April, 0.94 for 10 May, and 0.85 for 20 May for sites 1-8, with the low value on 20 May largely due to the bare-ground sites (ratio 0.72). For energy balance, the ratio should be unity. Twine et al. (2000) suggest that ratios less than unity are due to underestimates of H and LE. However, the small ratio on 20 May was probably also the result of standing water in the fields, which not only put the representativeness of the soil heat flux and net radiation into question,

* See http://www.atd.ucar.edu/sssf/facilities/class/class.html#Radiosonde

** Further information on the NCAR stations is available on the ATD/SSSF Web site (http://www.atd.ucar.edu/atd_data.html).

but locally changed the energy balance, so we will assume that measured $H + LE$ is ≈90% of its true value. The corresponding figures for the NOAA grass site are 0.94 for 10 May and 0.91 for 20 May. For a complete description of CASES-97 surface fluxes, see Yates et al. (2001).

2.2.5. *Synoptic Maps (Horizontal Gradients of* Θ *and* Q*)*
The synoptic maps used are products of the National Center for Environmental Prediction (NCEP) Eta 4-D Data Assimilation system (EDAS). The EDAS generates eight 3-hourly gridded analyses during each 24-hour period, based on observed data (Rogers et al., 1996). The horizontal resolution is 40 km and the vertical resolution 25 hPa to 2 km above ground level.

3. Description of Days Analysed

We choose 29 April, 10 May, and 20 May because of simple weather conditions and a range of surface conditions (Table I). There were scattered to broken cirrus on the morning of 29 April, clear skies on 10 May, and scattered cirrus on the morning of 20 May. Winds were steady during the morning on all three days: 10 m s^{-1} from the south on 29 April, 5–6 m s^{-1} from the SSW on 10 May, and 6-7 m s^{-1} from the ENE on 20 May. These three days exhibit a range of soil-moisture distributions and vegetative conditions. As noted in LeMone et al. (2000), the ground was dry on 29 April, due to no precipitation for over a week; near-surface soil moisture showed the most variability on 10 May, due to moderate rain (up to 60 mm locally, Brandes et al., 1999) 2 days prior; and the ground was saturated on 20 May, due to heavy rains (up to 90 mm locally) the day before. During CASES-97, the winter wheat grew steadily, and the grass changed from dormant to green. The average infrared radiometric surface temperature T_{ir} (higher for a larger fraction of dormant vegetation and dry soil) and its standard deviation σ_{Tir} (a measure of the horizontal contrast in vegetative cover and near-surface soil moisture) in Table I reflect the change in surface conditions during the field study; both are highest on 29 April and lowest on 20 May.

The precipitation pattern and spring greenup are reflected in the range of behaviour for H and LE according to surface cover, as illustrated in Figure 3. The 29 April surface fluxes show the greatest contrast, with LE over winter wheat four times that over bare ground. LE is intermediate over the mostly dormant grass sites. The largest surface heat flux and Bowen Ratio (H/LE, based on average H and LE) occur on 29 April, consistent with the dormant vegetation and dry soil. By 10 May, the grass had started greenup, but photographs suggest a large fraction was still dormant, so that there are still significant differences in fluxes related to land-cover category. Patchy near-surface soil moisture also contributes to horizontal variability. On 20 May, completion of greenup and wet soil lead to the lowest average H, the highest average LE, the least variation in H, and almost no

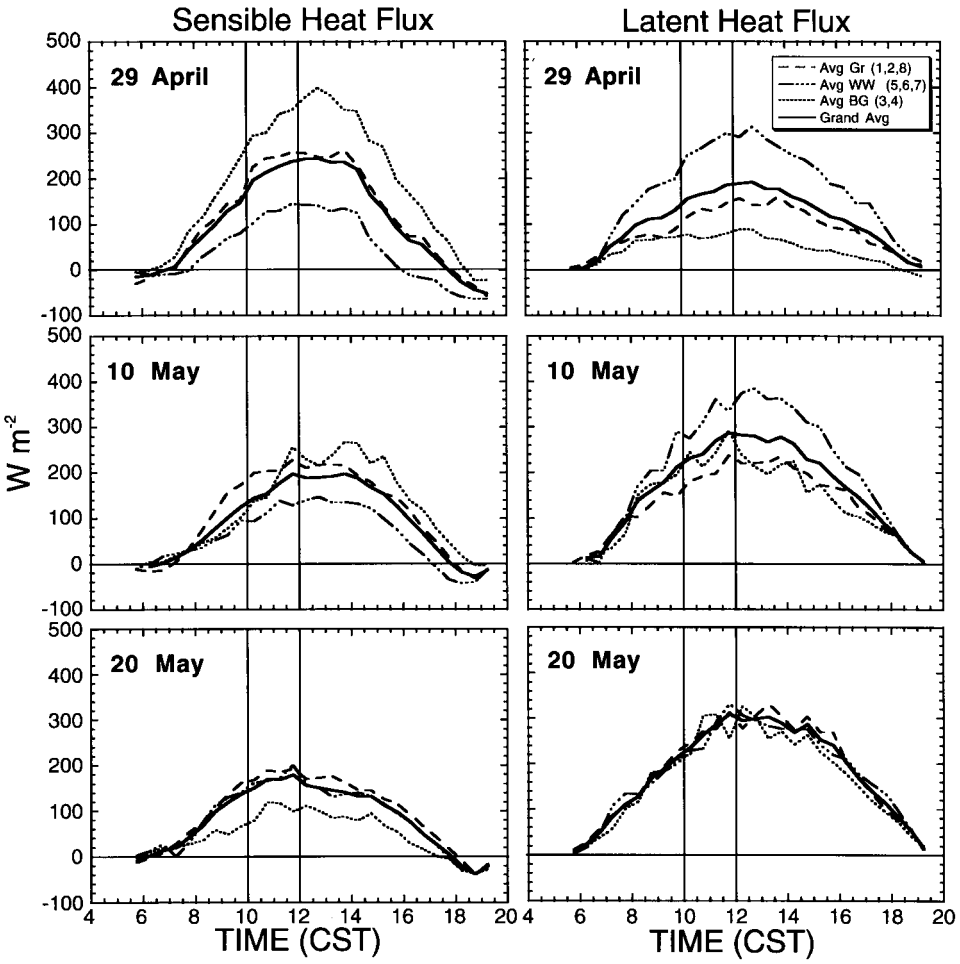

Figure 3. Latent heat (LE) and sensible heat (H) fluxes, averaged according to vegetation type, for the three days. Dashed line: Grass sites; dot-dash line: Winter wheat; dotted line: Bare ground; solid line: Grand average. The vertical lines denote beginning and ending times for budgets.

variation of LE by surface-cover category. On the other hand, H was lower over the bare-ground sites, probably reflecting the presence of standing water. While rainfall seemed to be a major factor here, Fitzjarrald et al. (2001) found that a decrease in daytime Bowen ratio with time is a good marker for spring greenup (in this case, leafing out of deciduous forests).

The 'daytime' (1000–1700 CST) behaviour of the temperature and specific humidity at 2 m, shown in Figure 4 for the eight NCAR sites, is distinct from the 'transition' behaviour before and after. In the early morning, air temperature varies with elevation, with the greatest range for 10 May, due to low wind speeds and extremely stable thermal stratification at sunrise (LeMone et al., 2000; LeMone and Grossman, 2000). Early-morning, and sometimes late-afternoon, peaks in

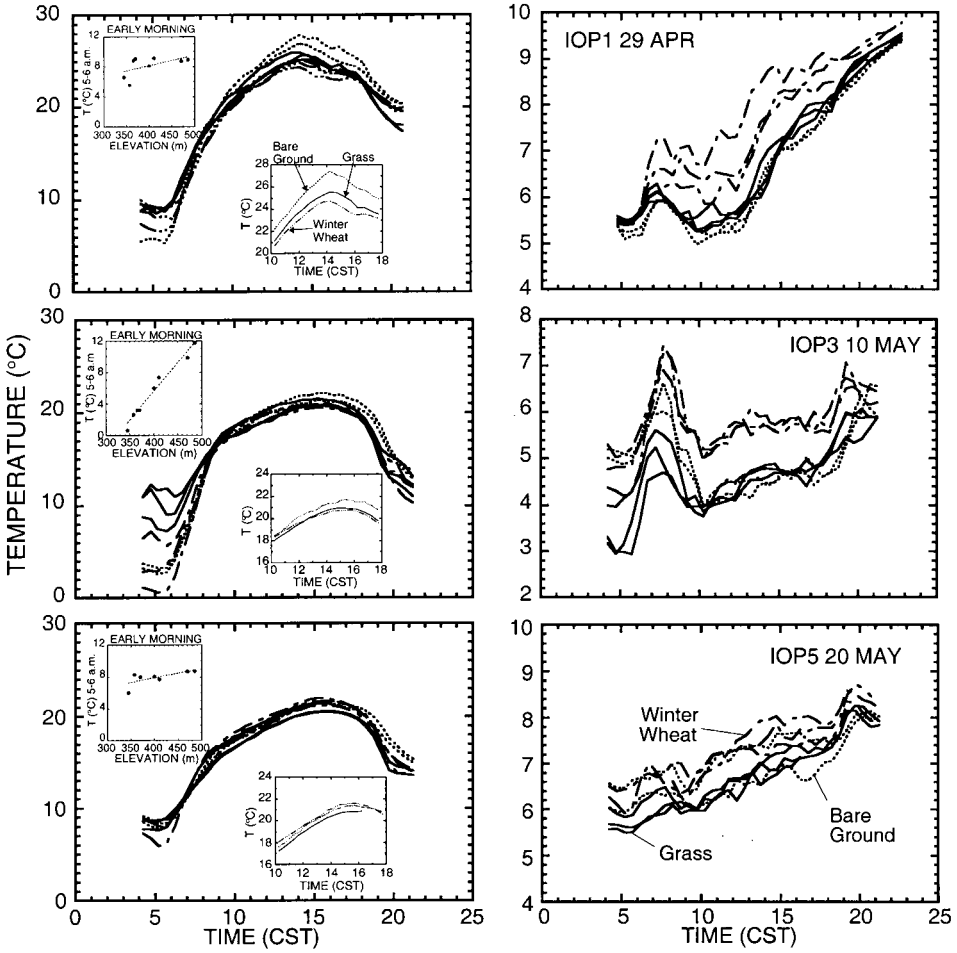

Figure 4. For the three days (left) temperature and (right) specific humidity at stations 1–8. For temperature: Left inset is temperature averaged from 0500–0600 CST as function of station elevation; right inset is temperature averaged according to ground cover. Solid lines: Grass; dotted lines: Bare ground; dot-dash lines: Winter wheat. Adapted from Figs. 14 and 16 of LeMone et al. (2000), with permission from the American Meteorological Society.

specific humidity are evident. These peaks result from the near-surface trapping of water vapour produced by evapotranspiration, lack of ventilation and stable thermal stratification (Geiger (1966) describes the morning and evening peaks and their explanation as well known). In contrast, the daytime temperature and specific humidity vary smoothly and are more clearly related to surface cover. As in the case of the fluxes, the greatest contrast by surface cover is on 29 April and the least on 20 May.

The mixed-layer depth h (Figure 5) is a function of conditions above the mixed layer as well as surface fluxes. At 1200 CST, h was shallowest on 20 May, reflecting

the largest static stability $\partial\Theta_v/\partial z$ above the mixed layer and the smallest surface virtual temperature flux ($\overline{w'T_v'}|_\circ = 0.15$ K m s^{-1} at noon) of the three days. 29 April had the largest $\overline{w'T_v'}|_\circ$ values (0.21 K m s^{-1} at noon), and $\partial\Theta_v/\partial z$ above the mixed layer was about the same as for 10 May, but warming of the overlying stable layer during the morning delayed mixed-layer growth. Thus, 10 May had the deepest noontime mixed layer in spite of intermediate $\overline{w'T_v'}|_\circ$ (0.17 K m s^{-1} at noon). Although the cases span nearly a month of time, the small number of cases and the number of factors influencing h preclude the identification of a seasonal pattern in h, as discussed in Freedman et al. (2001). The profiler h values are sometimes higher than the others because SNR responds mainly to vertical gradients in water vapour, while the sonde and aircraft h values mark the top of the layer with near-constant Θ and Q. The scatter in h reflects horizontal variation due to both large eddies (e.g., Hardy and Ottersten, 1969; Eloranta and Forrest, 1992) and terrain (LeMone et al., 2000).

4. Budget Calculations

4.1. Handling time changes

The times 1000–1200 CST were chosen for the budgets because (a) from the foregoing, the boundary layer changes rapidly even though the morning transition with its associated large horizontal heterogeneity is essentially over and (b) because morning aircraft measurements were generally between 0830 and 1230 CST. Accounting for this evolution is critical, because time changes can be interpreted as spatial changes. For example, as illustrated in Figure 6, uncorrected leg-averaged potential temperatures from a descending stack through the mixed layer during rapid warming produces an erroneous superadiabatic lapse rate. Thus, before we describe how each term in (1b) is calculated, we describe the three ways time changes are handled: The time-trend technique, the surface-normalisation technique, and the modified time-trend technique.

4.1.1. *Time Trend Technique (Fluxes and Means)*

Using plots of aircraft flux-leg altitude vs. time (e.g., Figure 7), we divide the flux legs into three or four layers. In the figure, we have four layers, two of which overlap. In each layer, the leg-averaged data are plotted as a function of time and fit to least-squares linear (fluxes) or quadratic (Θ and Q) curves. Because of possible inter-aircraft biases, the best-fit curves are computed separately for each aircraft, and the fluxes and time trends for the two aircraft averaged. The same procedure is applied to z/h, the average flux-leg height normalised by the mixed-layer depth at leg-centre time. The Q and Θ regression curves are then used to obtain $\partial Q/\partial t$ and $\partial\Theta/\partial t$ at 1000, 1100, and 1200 CST. Similarly, the flux and z/h curves are used to obtain flux vs. height at 1000, 1100, and 1200 CST. A linear fit to each flux profile

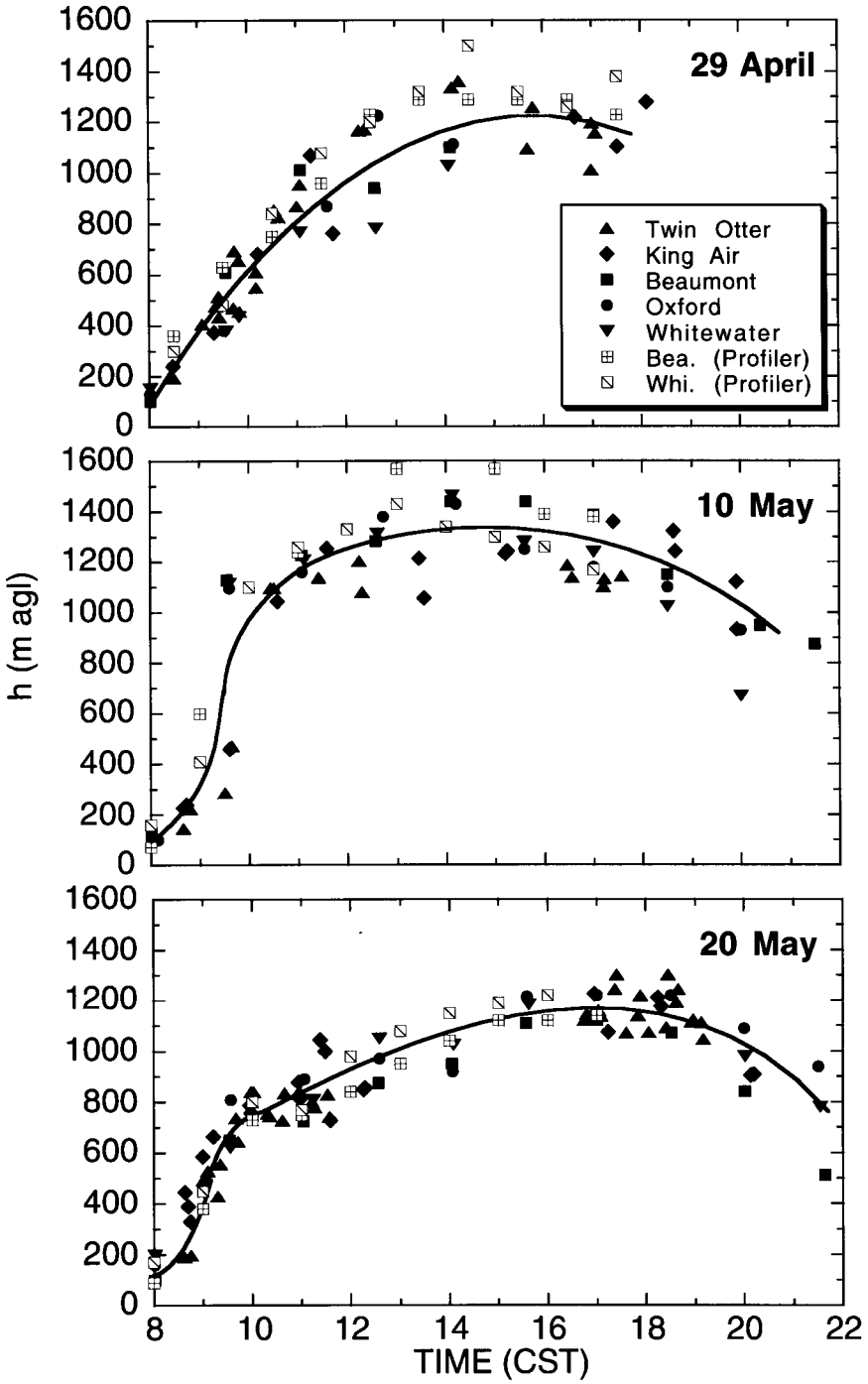

Figure 5. Mixed-layer depth h relative to the ground, as a function of time, for 29 April, 10 May, and 20 May. Solid symbols: From in-situ data (radiosondes at Beaumont, Oxford, and Whitewater; soundings from King Air and Twin Otter); open symbols: From radar wind profiler SNR.

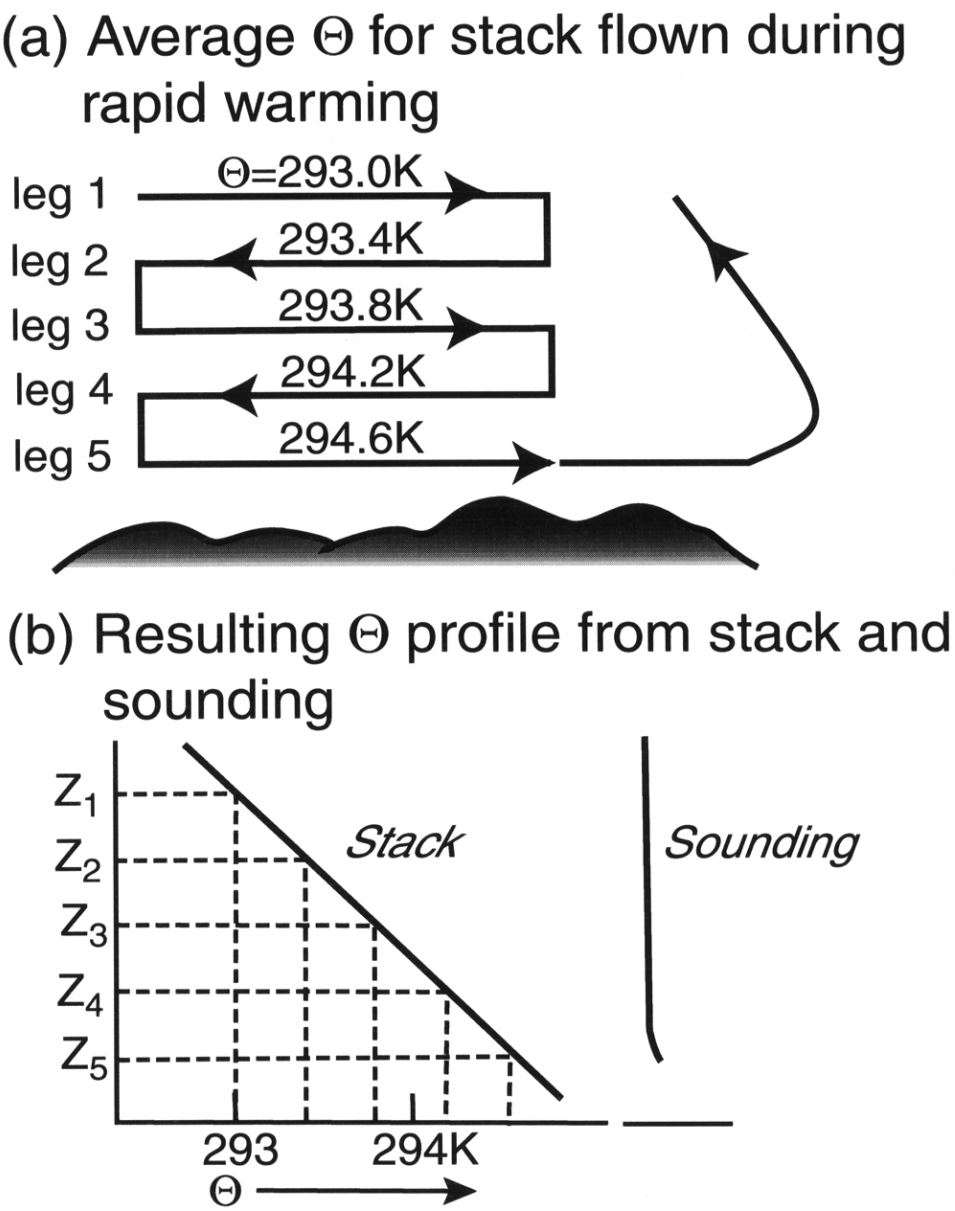

Figure 6. Schematic illustrating apparent vertical potential temperature gradient caused by warming. In the upper frame, the heavy lines are idealized stack pattern (flux legs at successively lower altitudes) followed by a rapid-ascent sounding; numbers are flight-leg averages. The bottom frame compares the uncorrected Θ profile to the Θ profile for the near-instantaneous sounding.

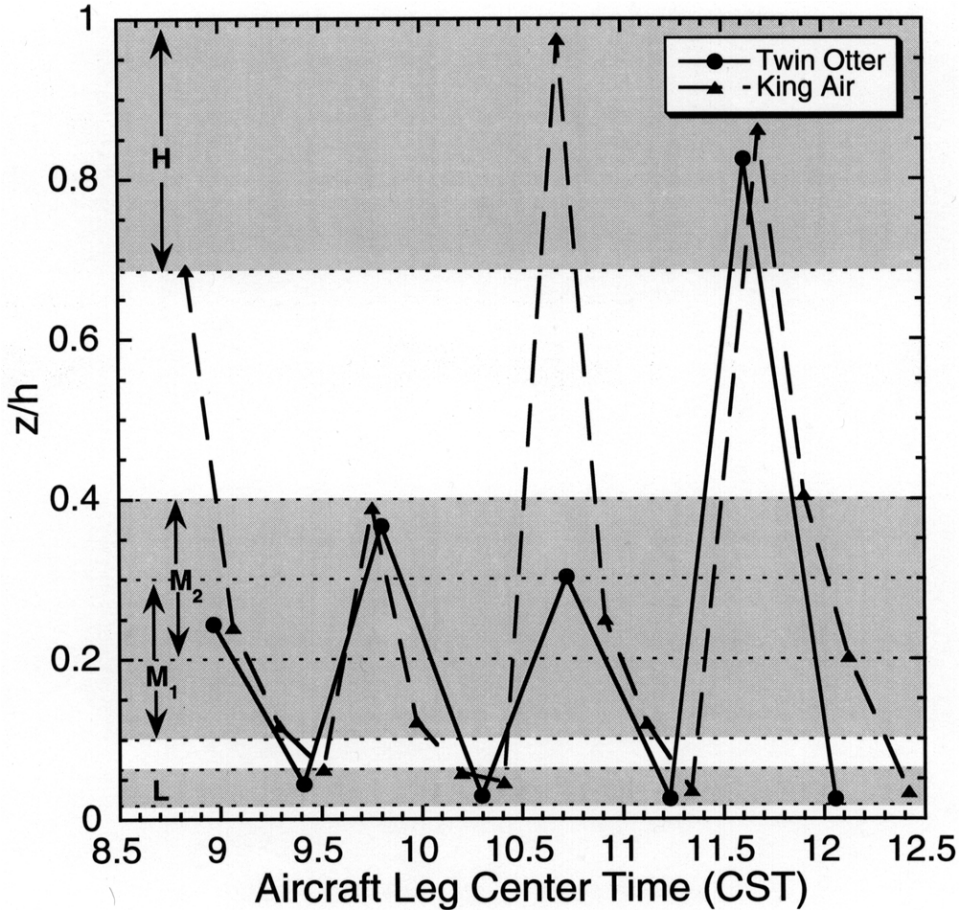

Figure 7. For 10 May 1997 stack patterns, aircraft flux-leg centre times vs. average aircraft flux-leg altitude (agl), normalized by mixed-layer depth h, for Twin Otter (solid) and King Air (dashed). The shaded layers indicate where data are combined to find time trends for fluxes and mean quantities; L = low, M = middle, H = high. Typical straight-and-level flight-leg durations were 8–16 min (≈30–60 km) for the Twin Otter, and 8–10 min (≈40–60 km) for the King Air.

provides the vertical flux divergence, which is converted to dimensional units using the corresponding mixed-layer depth. The disadvantage of this technique is having to base each profile on only 3–5 points in the vertical.

4.1.2. *Surface-Normalisation Technique (Fluxes)*

In this case, the leg-averaged fluxes at each height are normalised by the surface flux at the flux-leg centre time. The profiles are then divided into time blocks that have good vertical coverage from both aircraft. Each time block includes one King Air stack pattern, plus two or more Twin Otter legs. For each time block, a linear fit to the normalised fluxes plotted against z/h yields a non-dimensional vertical flux divergence, which is dimensionalised using the boundary-layer depth and surface

flux at the block centre time. The vertical flux divergences are then plotted as a function of time and subjected to a linear fit, which is used to assign flux-divergence values to 1000, 1100, and 1200 CST.

This technique assumes (a) that the flux at any height in the mixed layer responds instantly to the surface flux, and (b) the shape of the flux profile doesn't vary significantly over one time block. For example, if the heat flux decreases linearly with height to a constant fraction of its surface value at the top of the mixed layer, there would be no error introduced by using the surface fluxes to normalise the aircraft fluxes. It is also assumed that the same surface flux can be used to normalise the data from both aircraft tracks. Using 1-km land-surface-model (LSM)-based gridded fluxes* to estimate the surface fluxes beneath the pairs of flight tracks used on each day, we found the average fluxes beneath the tracks differed by only ≈5%. However, the surface-normalisation technique combines data from the two aircraft.

4.1.3. *Modified Time-Trend Technique (Fluxes)*

In applying this technique, used in LeMone et al. (1999) to estimate momentum fluxes for an evolving boundary layer, we calculated vertical flux divergences for the same time blocks used for the surface-normaliation technique. However, the flux for each leg was corrected to the block centre time using the time trend for the layer it occupies (already found for the time-trend technique). A least-squares linear fit to the corrected fluxes plotted as a function of height provides the flux divergence at the centre time. A linear fit to the resulting flux divergences plotted as a function of time provides values at 1000, 1100, and 1200 CST. This technique has the advantages of (a) having data at more altitudes and (b) not having to assume a constant shape profile that responds instantly to surface fluxes.

4.2. COMPUTATION OF THE TERMS IN (1b)

4.2.1. *Time Tendency*

Time tendencies were computed using surface, aircraft, and radiosonde data, plotted as a function of normalised height z/h at 1000, 1100, and 1200 CST, and then averaged. Figure 8 shows the data used to compute $[\Theta]$ and $[Q]$ trends for 1100 CST 29 April, and schematic curves drawn through the data to reflect the average structure. The surface trends are averages of values calculated from least-squares quadratic fits to the half-hourly temperature and specific humidities at the nine surface stations. Aircraft time tendencies are from flux-leg averages via the time-trend technique; or are based on quadratic and linear least-squares fits to vertical mixed-layer averages from soundings plotted as a function of time. Trends from vertically-averaged radiosonde data are based on quadratic fits using at least four sequential soundings at each site and then averaging the trends for the three sites.

* Fei Chen, David Yates, and Haruyasu Nagai (personal communication, 2001). These flux maps were generated from rainfall history, soil type, land use, etc., using the land surface model described in Chen et al. (1996).

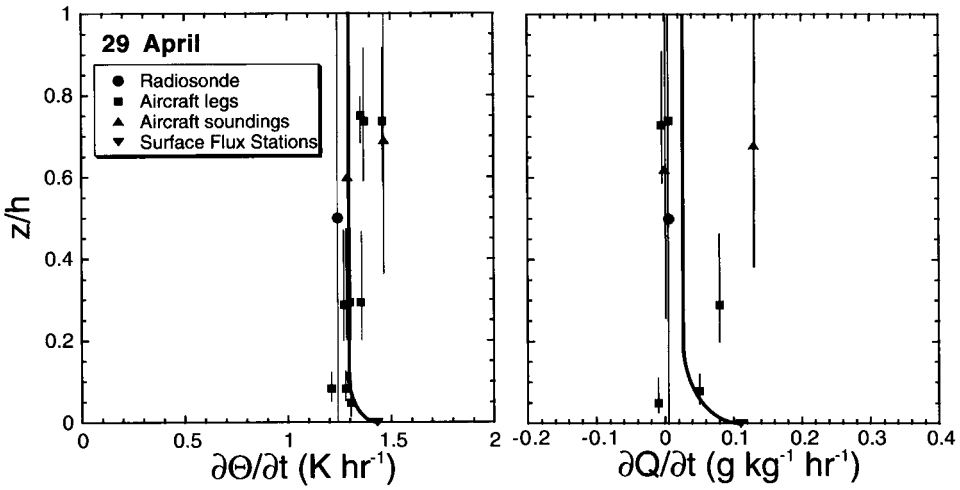

Figure 8. Mixed-layer time tendencies, $\partial\Theta/\partial t$ and $\partial Q/\partial t$ at 1100 CST 29 April, based on aircraft flux legs, aircraft soundings, radiosondes, and surface flux-site data. Vertical lines indicate average altitude range over which averages were evaluated. Heavy line represents schematic average vertical profile.

Table II summarises the time trends for Θ and Q for the three days. From the table, Θ at 2 m increases more rapidly than the mixed-layer average on all three mornings, consistent with development of a superadiabatic layer. The 2-m Θ trend is tied more closely to the mixed-layer Θ trend than to the radiometric surface temperature trend. Indeed, Θ at 2 m rises faster on 20 May than on 10 May even though the radiometric surface temperature rises more slowly. LeMone et al. (2000) note that the slower 2-m Θ rise on 10 May is tied to spreading the heating through a deeper mixed layer (see Figure 5). On all three days, the mixed layer was drying at 1000 CST and moistening thereafter, a trend reflected at 2 m on 29 April and 10 May but not 20 May.

4.2.2. *Flux Divergence*

Flux divergence was computed using all three techniques (Section 4.1) to account for time evolution. Figures 9a and b show examples of temperature and humidity-flux profiles for the four stacks on 10 May and the resulting divergences, based on the modified time-trend technique. To increase sample size, we use pairs of time blocks to estimate the vertical gradient $\partial\overline{w'\theta'}/\partial z$; the scatter is so large for mixing-ratio fluxes, that all the flux legs are combined to obtain a single estimate of $\partial\overline{w'q'}/\partial z$ at 1100 CST.* Objective fits of the vertical flux profiles based on the three techniques are obtained with and without surface fluxes; so use of the three

* The scatter results partially from the fluxes reaching a maximum at mid levels for some stacks. Because of this, we recomputed the flux profiles using quadratic best fit and then taking the resulting flux divergence across the mixed layer; the flux divergence values did not differ significantly from those using the linear fits.

TABLE II

Time tendencies for temperature and mixing ratio, based on aircraft flux legs and soundings, radiosondes, and surface data.

(a) Mixed layer

Date	$\partial[\Theta]/\partial t$ (K hr^{-1})			$\partial[Q]/\partial t$ (g kg^{-1} hr^{-1})		
	1000 CST	1100 CST	1200 CST	1000 CST	1100 CST	1200 CST
29 Apr	1.50 ± 0.12	1.29 ± 0.07	1.08 ± 0.11	-0.06 ± 0.05	0.05 ± 0.05	0.15 ± 0.10
10 May	0.78 ± 0.15	0.69 ± 0.08	0.59 ± 0.09	-0.08 ± 0.05	0.10 ± 0.03	0.17 ± 0.03
20 May	0.97 ± 0.05	0.90 ± 0.05	0.84 ± 0.10	-0.03 ± 0.05	0.10 ± 0.05	0.11 ± 0.04

(b) Surface stations (2 m)

Date	$\partial\Theta/\partial t$ (K hr^{-1})			$\partial Q/\partial t$ (g kg^{-1} hr^{-1})		
	1000 CST	1100 CST	1200 CST	1000 CST	1100 CST	1200 CST
29 Apr	1.82	1.43	1.20	−0.06	0.11	0.25
10 May	1.07	0.85	0.65	−0.23	0.11	0.20
20 May	1.07	0.93	0.83	0.21	0.24	0.16

(c) King-Air radiometric surface temperature

Date	$\partial T_{\mathrm{sfc}}/\partial t$ (K hr^{-1})		
	1000 CST	1100 CST	1200 CST
29 Apr	4.52	3.33	2.14
10 May	4.19	3.02	1.84
20 May	3.72	2.83	1.93

procedures leads to six estimates of flux divergence at each budget time. These divergences are averaged to form a 'consensus' value.

Figures 9 (bottom frames), 12 and 13 show the random-error estimates for the three days, based on Mann and Lenschow (1994) and using the Lenschow and Stankov (LS, 1986) integral scale formulation; the numbers are multipliers needed to account for the observed flux integral scales, found from frequency-weighted spectra as described in Lenschow (1995). The sets of flux legs used to estimate the random error are the same as those used to estimate the vertical flux divergence. The standard deviations based on averaging the six flux-divergence estimates are about half the LS uncertainties.

There appears to be a systematic bias between the θ fluxes from the two aircraft. Figure 10 shows $\overline{w'\theta'}$, normalised by the surface flux at the leg centre times, as a function of z/h for the three days. Note that the vertical heat flux divergence from the King Air is smaller than that sampled by the Twin Otter by about 30%. It is unlikely that the differences in fluxes are real, since the estimated surface fluxes

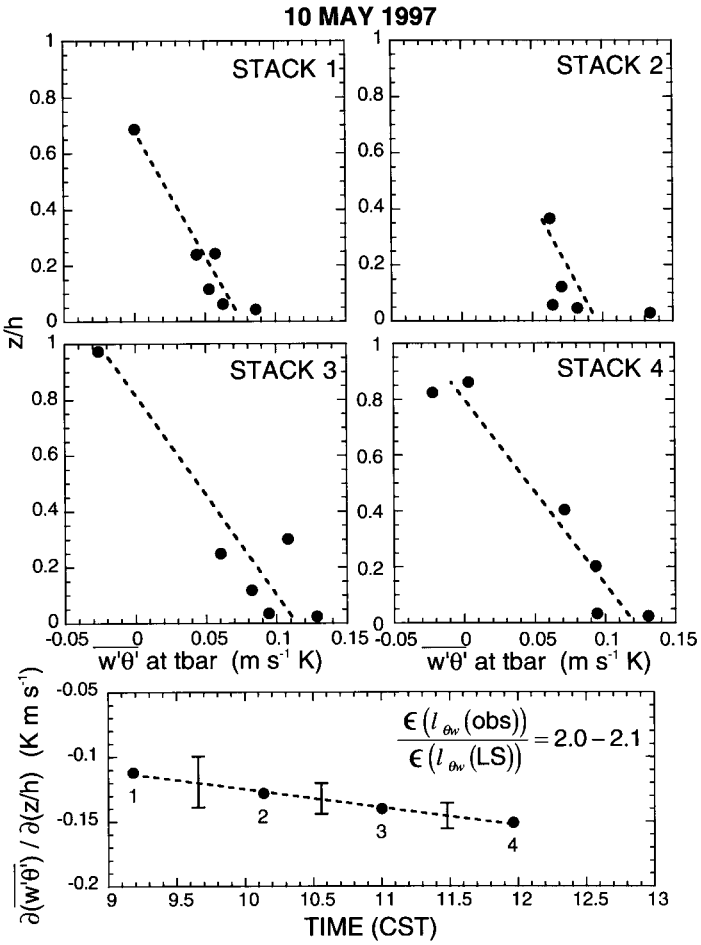

Figure 9a.

Figure 9. For 10 May, vertical profiles of leg-averaged fluxes corrected to stack-centre time using modified time-trend technique; the bottom frames show the trend in vertical flux divergence, for (a) $\overline{w'\theta'}$, and (b) $\overline{w'q'}$; tbar is centre time for data in each frame. In bottom frame, error bars are based on Mann and Lenschow (1994) with integral scales $l_{w\theta}$ and l_{wq} according to Lenschow and Stankov (LS, 1986), using pairs of stacks for θ, and all flux-leg data for q; ratios compare error estimated using actual flux integral scales to the error using LS integral scales; points are numbered according to corresponding stack(s) in upper frames.

beneath the two aircraft tracks* using the LSM-based flux maps (footnote *, page 18) were within 5%. Since we do not know which aircraft is correct, we do not

* On 29 April and 10 May, the Twin Otter flew the flight track just to the north of Beaumont in Figure 2, while the King Air flew that track on 20 May. The southernmost leg in Figure 2 was flown by the King Air on 29 April and 10 May, while the Twin Otter flew an east-west leg that crosses Site 10 on 20 May.

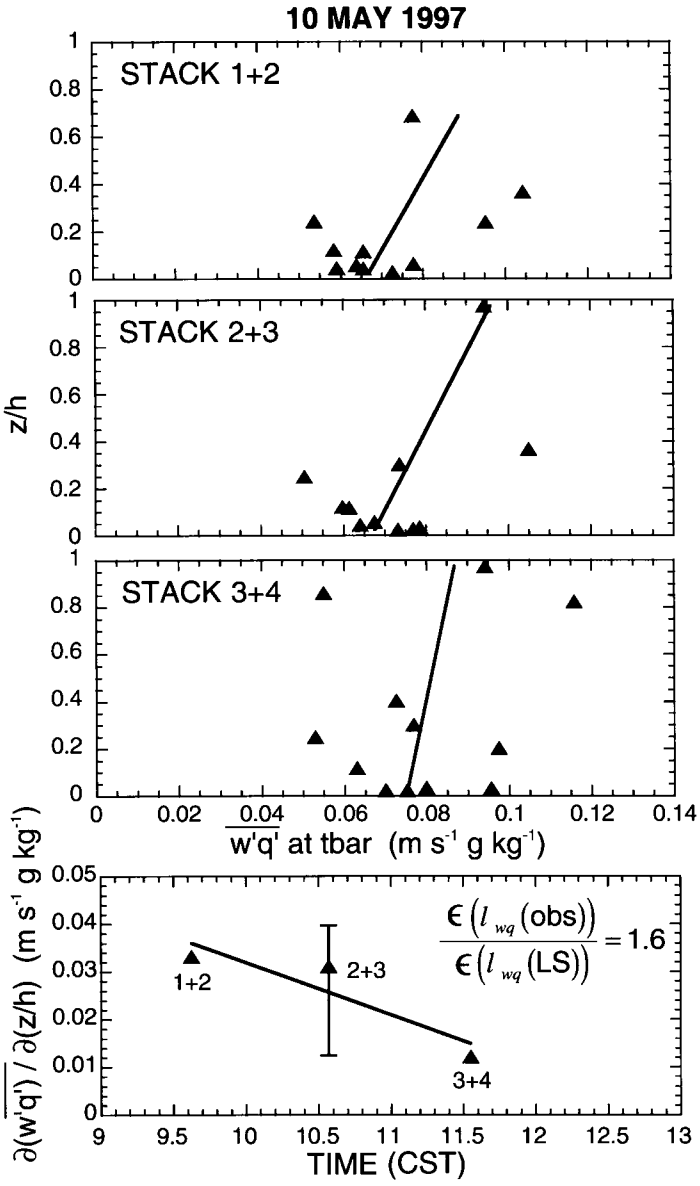

Figure 9b.

adjust the flux data for either aircraft. We return to the bias problem in the budget discussion.

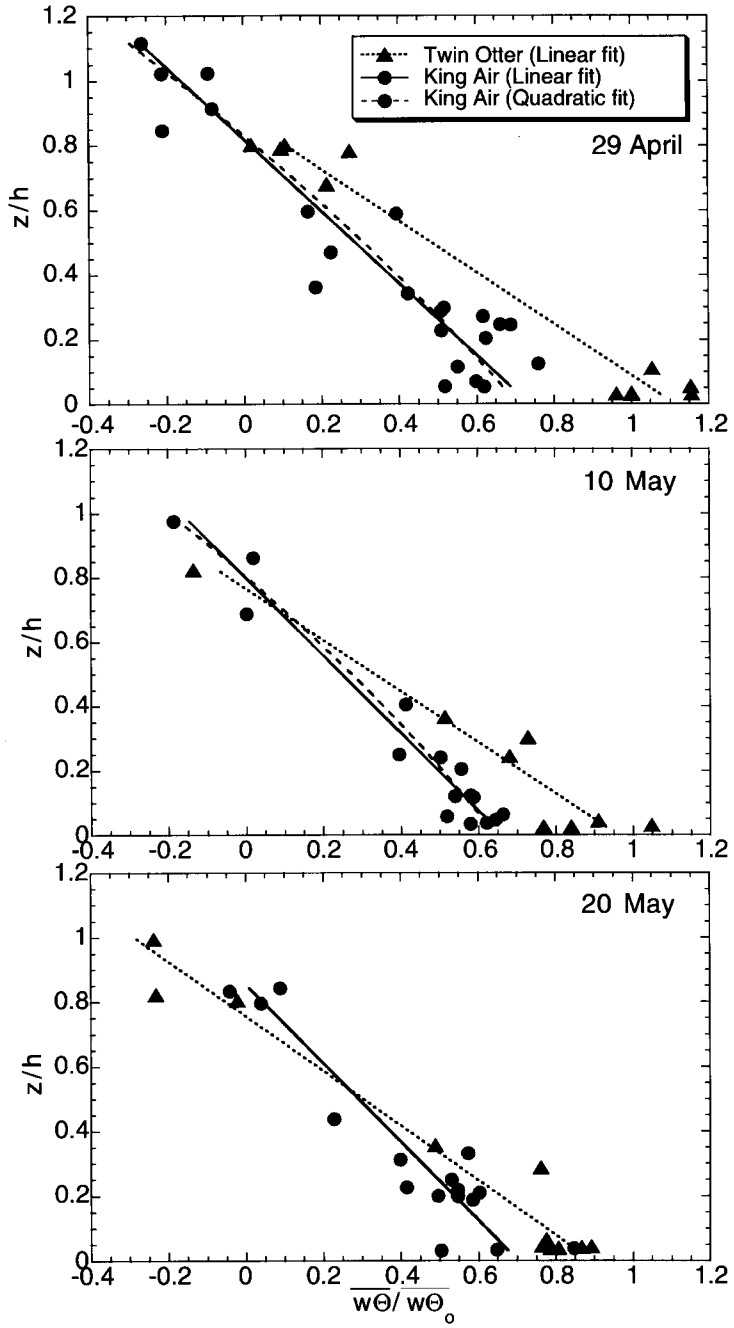

Figure 10. For Twin Otter and King Air morning flux legs on 29 April, 10 May, and 20 May, $\overline{w'\theta'}/\overline{w'\theta'}|_o$ as a function of z/h. Each point represents $\overline{w'\theta'}$, averaged over a flight leg and normalized by the average surface flux $\overline{w'\theta'}|_o$ at leg-centre time, with leg height z normalized by h at leg-centre time. Solid and dotted lines are least-squares linear fit; dashed lines show best-fit quadratic to King Air data; the quadratic fit for 20 May is not distinguishable from the linear fit.

TABLE III

$\Delta\Theta/\Delta Q$ across the transition layer, based on morning to early-afternoon data.

Date	Number of soundings	Sonde $\Delta\Theta/\Delta Q$ (K g^{-1} kg)	Number of soundings	Aircraft $\Delta\Theta/\Delta Q$ (K g^{-1} kg)
29 April	9	1.54 ± 0.68	11	1.16 ± 0.29
10 May	11	0.95 ± 0.17	10	0.71 ± 0.13
20 May	14	0.83 ± 0.31	18	0.87 ± 0.07*

* Because of time variation, this average was based on six soundings near 1100 CST.

Because of the large scatter in humidity fluxes, we also estimated $\overline{w'q'}$ at the mid-entrainment layer or z_i ($\approx h$+100 m) from radiosonde and aircraft soundings, following Betts (1992) and Betts et al. (1992), i.e.,

$$\overline{w'q'}_{zi} \approx \frac{\overline{w'\theta'}_{zi}}{\Delta\Theta/\Delta Q}. \tag{2}$$

The ratios $\Delta\Theta/\Delta Q$ appear in Table III. $\Delta\Theta$ and ΔQ are the differences between the mean mixed-layer value and the free-atmosphere value, defined as where a straight line through the θ or q profiles in the lowest few hundred metres of the free atmosphere intersects the top of the entrainment layer. The entrainment layer is where the vertical gradients of q and θ are large compared to above and below. Scatter was particularly large on 29 April, because of complex structure in the moisture field above the mixed layer. Error estimates are found by subtracting (2) with 'true' values of $\overline{w'\theta'}_{zi}$ from (2) with 'true' values perturbed by uncertainties $\epsilon(\Delta\Theta/\Delta Q)$ and $\epsilon(\overline{w'\theta'}_{zi})$ with the sign of ϵ defined to maximize the error. We use Table III to estimate $\epsilon(\Delta\Theta/\Delta Q)$, and estimate $\epsilon(\overline{w'\theta'}_{zi})$ from z_i and the uncertainty in the vertical flux divergence. We do not account for the uncertainty associated with the choice of z_i, so the error estimates for $\overline{w'q'}_{zi}$ could be low.

4.2.3. *Large-Scale Advection*

Horizontal winds are found from both profiler data and from the aircraft stack patterns. Horizontal gradients are found from aircraft tracks, radiosondes, and EDAS synoptic maps.

The wind vector in the advection term is the average of the mean mixed-layer wind vector from the King Air flux stacks and that from the three profilers. For each dataset, the winds at the budget times are based on a least-squares linear fit to the mixed-layer averaged wind components vs. time. Table IV compares the winds and shows them to be within 1 m s^{-1} of each other, in spite of representing different averaging procedures and slightly different locations. Since we use the mean of these two values, the uncertainty is of the order of 0.5 m s^{-1}.

TABLE IV

Comparison of average winds from profilers and aircraft flux stacks.

Date	$[U]$ (m s^{-1}) (Profiler, Aircraft)			$[V]$ (m s^{-1}) (Profiler, Aircraft)		
	1000 CST	1100 CST	1200 CST	1000 CST	1100 CST	1200 CST
29 April*	1.02, 0.05	−0.05, −0.39	−1.11, −0.83	9.50, 8.54	10.07, 8.84	10.65, 9.14
10 May	1.30, 0.40	1.00, 0.00	1.00, 0.00	5.00, 4.00	5.50, 4.25	5.75, 4.25
20 May	−6.63, −6.60	−6.38, −6.76	−6.13, −6.92	−0.41, −0.95	−0.44, −1.22	−0.46, −1.49

* Profiler average from Whitewater and Beaumont only.

Gradients from aircraft triangle patterns were calculated using the three possible combinations of two flight tracks and then averaged. For each track pair, two simultaneous equations relate zonal and meridional gradients $\partial\Psi/\partial x$ and $\partial\Psi/\partial y$ to the gradients estimated along the two tracks, $\partial\Psi/\partial s_1$ and $\partial\Psi/\partial s_2$:

$$\frac{\partial\Psi}{\partial s_1} = \frac{\partial\Psi}{\partial x}cos\phi_1 + \frac{\partial\Psi}{\partial y}sin\phi_1 \tag{3a}$$

$$\frac{\partial\Psi}{\partial s_2} = \frac{\partial\Psi}{\partial x}cos\phi_2 + \frac{\partial\Psi}{\partial y}sin\phi_2, \tag{3b}$$

where ϕ_1 and ϕ_2 are two flight-track angles (for triangle legs, $|\phi_1 - \phi_2| \approx 60°$), and $\partial\Psi/\partial s_i$ is found using a least-squares linear fit of Ψ vs time for leg i, correcting for time change $\partial\Psi/\partial t$ and then multiplying by the ratio of elapsed time to distance. We assume that the gradients thus obtained are consistent with those averaged over the mixed layer.

Gradients from the sondes are also found from (3), with $\partial[\Psi]/\partial s$ estimated from pairs of sonde stations (1,2),

$$\left(\frac{\partial[\Psi(t)]}{\partial s}\right)_{1,2} = \frac{[\Psi_2(t)] - [\Psi_1(t)]}{\Delta s_{12}}, \tag{5}$$

where Δs_{12} is the distance between the sonde stations and $[\Psi(t)_i]$ is the mixed-layer average of Ψ at station i and time t found from a quadratic least-squares fit of $[\Psi_i]$ as a function of time. A sequence of 4-6 sondes (3–4.5 hours) at each station is used for such estimates.

Synoptic gradients are based on EDAS synoptic maps of Θ and Q, at 950, 925, 900, and 850 hPa, for 1000, 1100, and 1200 CST. The 1000 and 1100 CST analyses are interpolated from the 0900 and 1200 CST analyses. The gradients are estimated across a box outlining the CASES-97 domain on the maps, and then vertically averaged from 950 hPa (close to surface pressure) to the pressure at h.

The uncertainty for the large-scale advection term ϵ_{adv} is approximated from:

$$\epsilon_{adv} \sim \left[\frac{\partial\Psi}{\partial x_i}\right]\epsilon_{[Ui]} + [U_i]\epsilon_{[\partial\Psi/\partial xi]}, \tag{6}$$

where $U_i = (U, V)$, $x_i = (x, y)$, and the average gradient through the mixed layer $[\partial\Psi/\partial x_i]$ is assumed equal to the average gradient measured at a height within the mixed layer $\partial\Psi/\partial x_i$.

In Appendix A, we show that the expected error from a single triangle pattern, $\epsilon_{[\nabla\Psi(a\triangle)]}$, is

$$\epsilon_{[\nabla\Psi(a\triangle)]} = 2^{\frac{1}{2}}\epsilon_{[\partial\Psi/\partial s]}, \tag{A9}$$

where $\epsilon_{[\partial\Psi/\partial s]}$ is the gradient uncertainty for a flight leg along one side of the triangle, assumed equal for the three sides. For CASES-97 triangle patterns, (A9) yields an average uncertainty of ≈0.34 K (100 km)$^{-1}$ for Θ and 0.33 g kg^{-1}(100 km)$^{-1}$m^{-1} for Q – in both cases, about a third of the observed gradients. These values, found following Lenschow et al. (1980) with integral scale $l_\Psi = h$, are comparable to the standard deviations for the best-fit lines through $\partial\Psi/\partial x_i(a\triangle)$; and the differences between triangle estimates of gradients along the flux-leg heading and the actual values from the flux legs are within these uncertainties for all variables except for Θ on 29 April and 20 May (King Air only). Unfortunately, the triangle patterns were typically flown between 1830 and 2300 CST, so that the gradients had to be extrapolated in time for 29 April and 10 May; thus uncertainties for 29 April and 10 May are based on the extrapolation uncertainty (see Appendix A). Since the flux legs were parallel to the wind on 20 May, gradients and uncertainties were computed using the flux legs and the first triangle pattern. In this case, the observed and assumed integral scales were similar.

We also combine aircraft and sondes to estimate $\nabla[\Theta]$ even though sonde uncertainties are significant. For $\epsilon_\theta = 0.2$ K, four triangles of three radiosondes (subscript r) provide gradients with an uncertainty $\epsilon_{[\nabla\Theta,r]} \approx 0.65\times$ K (100 km)$^{-1}$, of the same order as the uncertainty in extrapolated gradients from the aircraft triangles for 29 April and 10 May, and twice that for a single aircraft triangle (Appendix A, Tables AI, AII). The reasonable comparison of gradients from interleaved sonde and aircraft triangles (Figure A1), is consistent with using $\epsilon_\theta = 0.2$ K. Further, the sondes represent true vertical averages, while the aircraft triangle patterns are flown at one altitude. The uncertainty in aircraft-plus-sonde $[\Theta]$-gradients is estimated from

$$\epsilon_{[\nabla\Theta]} \sim \frac{\left(\epsilon^2_{[\nabla\Theta,r]} + \epsilon^2_{[\nabla\Theta,a]}\right)^{\frac{1}{2}}}{2}, \tag{6}$$

where the subscripts r and a denote radiosondes and aircraft, and it is assumed that $\epsilon_{[\nabla\Theta,r]}$ is not significantly different from $\epsilon_{[\nabla\Theta,a]}$. In contrast, even assuming ϵ_q =2%, the uncertainty in $\nabla[Q]$ from sondes is three to four times that for extrapolated gradients, and three times the uncertainty of a single aircraft triangle. Thus we compute horizontal $[Q]$ gradients using aircraft only.

4.2.4. *Radiative Flux Divergence*

Radiative flux divergences were computed by applying the Fu-Liou (1993) algorithm to the 0930, 1100 and 1230 CST soundings at Beaumont, Oxford, and Whitewater. Climatological values of CO_2 and other radiatively-active trace gases were used. GOES satellite images and mm-wave (33 GHz) cloud radar echoes at the ARM SGP-CART site (Lamont, Oklahoma) indicated cirrus between 0900 and 1230 CST on 29 April, cloudless skies on 10 May, and thin cirrus on 20 May, consistent with aircraft observers' reports. In the computations for 29 April, cirrus

clouds were assumed where sounding relative humidities reached 40% relative to water saturation, following Ou et al. (1995). 10 and 20 May were treated as cloudless. As an example, Figure 11 shows the boundary-layer temperature and dew point, radiative heating, and error estimates for the Oxford 1230 CST 20 May sounding. The uncertainty in solar, infrared, and net heating was estimated by perturbing the sounding by the uncertainties in temperature ($\pm$0.2 K, $\pm$0.5 K) and humidity ($\pm$2%, $\pm$5%). As seen from the figure, the errors are small in the mixed layer.

A greater source of uncertainty is the potential contribution to heating by boundary-layer aerosols. We estimated the effect of aerosols separately using a parameterisation of shortwave absorption by carbonaceous aerosols, developed by McKeen and described in Angevine et al. (1998b). This parameterisation is based on a rural aerosol model of absorption (single scattering albedo = 0.85) and scattering within a standard atmosphere to calculate the heating rate from aerosol using the discrete ordinate method of Stamnes et al. (1988) for 162 spectral intervals between 300 and 5000 nm. Calculated average boundary-layer heating rates were then parametrically fit to functions of the boundary-layer depth, zenith angle, and visibility, where visibility is related to aerosol extinction by Koschmeider's formula and assumed constant through the mixed layer. For the zenith angle and mixed-layer conditions here, the parametric calculations differ from the detailed calculations by less than 5%.

Since the synoptic reports list all visibilities $\geq$16 km as 16 km, we used King Air forward-looking videos to estimate visibility. The video-based visibilities are approximately 18.6 km for 29 April, 16.7 km for 10 May, and 20 km for 20 May. These visibilities are almost certainly too small due to poor video resolution, and apparent changes in visibility with height probably affect the estimates. However, the visibilities appear to be correct in a relative sense. Twin-Otter condensation-nuclei (CN) concentrations were higher on 10 May than 20 May, consistent with lower visibility on 10 May. Further, we expect lower visibility on the first two days due to agricultural burning. Finally, CN concentration maps for 10 May show a plume possibly originating from an oil refinery to the south. For comparison, median mid-day visual ranges in the south central U.S. from photometric data and nephelometry are between 24 and 40 km for this time of year (NAPAP, 1990).

5. Results

5.1. MIXING-RATIO (Q) BUDGETS

Figure 12 shows the time-tendency, large-scale horizontal advection, and vertical flux divergence terms in (1b), with the remaining terms included in the residual. While budget estimates are shown for all three times, the symbols and errors apply to 1100 CST only; values at 1000 and 1200 CST must be interpreted with caution.

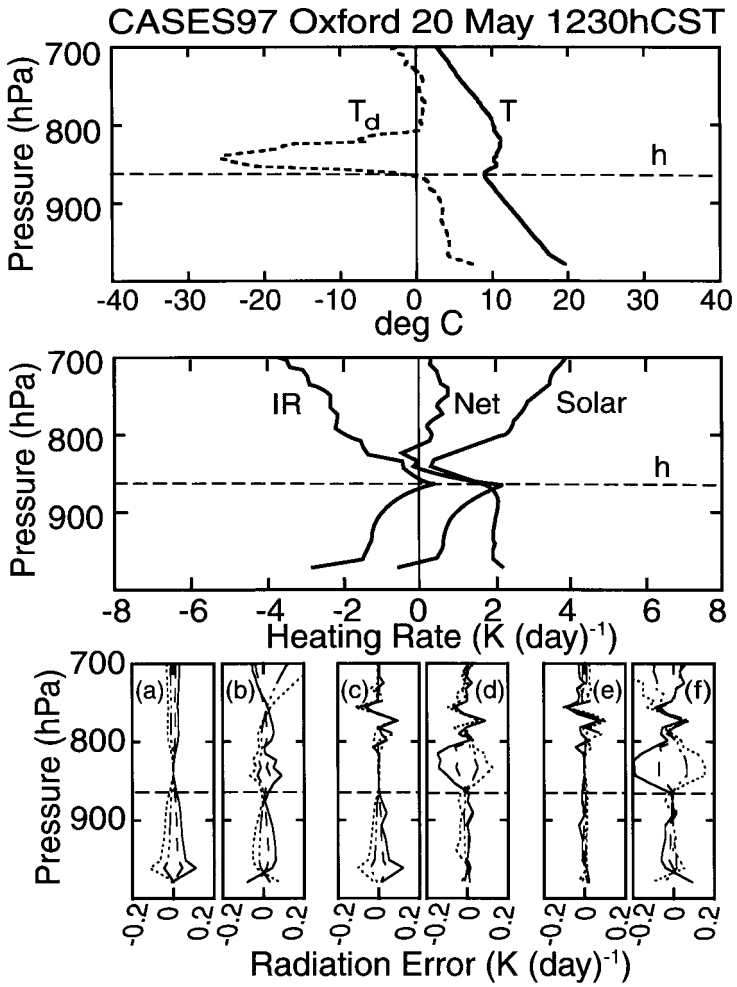

Figure 11. Radiation calculations using Fu-Liou (1993) code for the Oxford 20 May 1230 CST sounding. Top frame: Temperature and dew point in lower troposphere; middle frame: Calculated heating; bottom frame: Error estimates for sonde temperature uncertainties $\epsilon_\theta = \pm 0.2$ and ± 0.5 K and relative humidity uncertainty $\epsilon_q = \pm 2\%$ and $\pm 5\%$. In the bottom frame errors in: (a) infrared heating due to ϵ_θ, (b) infrared heating due to ϵ_q, (c) net heating due to ϵ_θ, d) net heating due to ϵ_q, (e) solar heating due to ϵ_θ, (f) solar heating due to ϵ_q. Solid line: -0.5 K or -5 %; dotted line: $+0.5$ K or $+5$ %; dashed line: -0.2 K or -2 %; dot-dash line: $+0.2$K or $+2\%$. Mixed-layer averages for net heating are in K day^{-1}: $\epsilon_q = -2\%, -5\%$: 0.006, 0.008; $\epsilon_q = +2\%, +5\%$: -0.012, -0.030; $\epsilon_\theta = -0.2$K, -0.5K: 0.015, 0.039; ϵ_θ = 0.2 K,0.5 K: -0.015, -0.039. Even the largest errors are less than 5% of the values in Table IV.

The budgets for all three days balance to within the large statistical error, with the exception of the 10 May budget with synoptic advection.

As observed previously for morning mixed-layer budgets (Grossman, 1992; Betts et al., 1992) drying is followed by moistening. On 29 April and 10 May, the drying is associated with positive $\partial\overline{w'q'}/\partial z$ – engulfment of dry air from above outweighs moistening from below (e.g., Grossman and Gamage, 1995), but the error bars are large. The 'anomalous' negative value of $\partial\overline{w'q'}/\partial z$ (moistening) at 1100 CST on 20 May in the figure is supported by negative values from (2) (Table V). This moistening reflects the fact that rapid mixed-layer growth, normally associated with drying, was over by 1000 CST (Figure 5). Also, LE was largest on this day (Figure 3), the surface layer was already moistening at 1000, and the mixed-layer drying was the smallest (Table II).

The advection term is most significant on 29 April, reflecting northward transport of moisture by strong winds from the south. There are significant differences between synoptic horizontal gradients and those estimated from aircraft data on 29 April and 10 May. If real, these differences may result from the heterogeneous surface or subsynoptic variation from other sources. As noted by Lilly (1983) and others, water vapour exhibits large variability on subsynoptic scales because it is largely a passive tracer. On 10 May, however, there was considerable curvature in the synoptic Q contours over the CASES-97 array, magnifying the potential for error in ∇Q; and the heterogeneity suggests that assuming an integral scale $\approx$h leads to too small a value for $\epsilon_{[\nabla Q]}$. In contrast, the advection terms from aircraft and EDAS synoptic maps are similar and small for 20 May, the day with more uniform surface conditions.

Table V compares the vertical flux divergences in Figure 12 to those from (2) and those needed to balance the budget exactly for horizontal advection based on both aircraft and synoptic estimates of $\nabla[Q]$. Calculations are based on $\overline{w'\theta'}|_{zi}$ from the Twin Otter (TO) alone as well as for both aircraft because of the potential bias problem illustrated in Figure 10. The flux divergences thus obtained reduce the residual for both $[Q]$ budgets on 20 May, and for the synoptic budget on 10 May (bold-face values in the table). However, except for 20 May, the estimated uncertainties in the vertical flux divergence are comparable to or greater than those in Figure 12 using the integral scales based on observations. Furthermore, the uncertainty estimates for flux divergences using (2) are conservative because they do not account for uncertainty associated with the choice of z_i.

5.2. Potential temperature (Θ) budgets

Figure 13 shows the time-tendency, large-scale advection, vertical flux divergence, and residual terms in (1b) for the three days. Three columns are included to represent the different ways of evaluating horizontal advection: using aircraft data, aircraft plus radiosonde data, and synoptic maps.

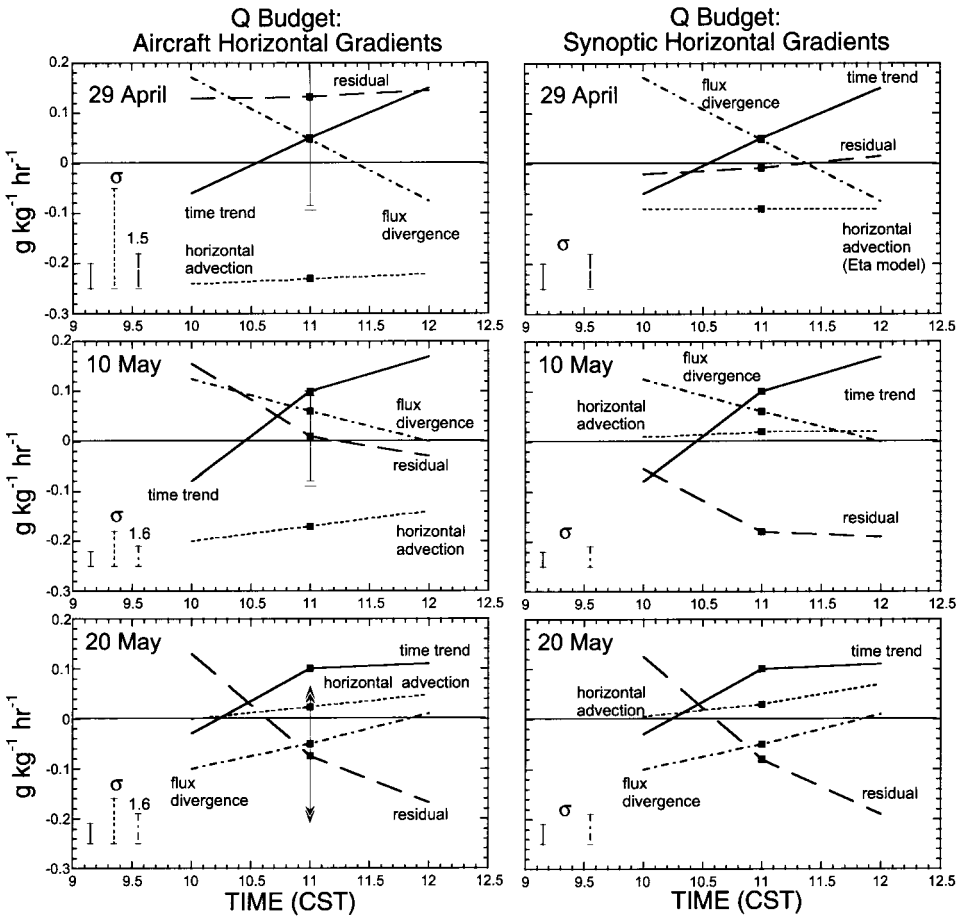

Figure 12. For the budget (1b) for mean mixed-layer mixing ratio $[Q]$, time-tendency (solid line), flux-divergence (dot-dash), horizontal advection (short dash), and residual (long dash); using advection with ∇Q from aircraft data only (left column), and from synoptic maps (right column). Square symbols are for budget at 1100 CST; values at 1000 and 1200 CST are uncertain and should be interpreted with caution. Magnitudes of the error estimates at 1100 CST are indicated by vertical lines beneath the σ symbol, using same scale and line convention as for curves representing budget terms; the numbers next to the σ symbol are ratios of flux-divergence error estimated from the observed integral scales to those used in Lenschow and Stankov (1986). Error bars on the residual curve are root sum squares of individual-term errors; the smaller value is for flux-divergence error based on Lenschow–Stankov integral scales, and the larger value is for flux-divergence error based on observed integral scales. 20 May error denoted by arrows because of unknown (probably small) error associated with assuming flux legs are along wind. Error was not estimated for synoptic gradients.

TABLE V

Comparison of $\overline{\frac{\partial w'q'}{\partial z}}$ (g kg^{-1} hr^{-1}) from Figure 12 to values needed to balance the budget for horizontal advection with $\underline{\nabla[Q]}$ from aircraft or synoptic maps, and to values obtained from $\overline{w'q'}|_{zi}$ based on (2) and $\overline{w'\theta'}|_{zi}$ from both aircraft or from the Twin Otter (TO), and surface fluxes estimated from flux towers and aircraft.

Date	Surface flux from towers		Surface flux from aircraft		Uncertainty	Figure 12	Need (A/C Adv)	Need (Syn. Adv)
	Both	TO	Both	TO	Both			
29 April	−0.09	−0.09	−0.08	−0.08	0.16 (0.10)*	+0.05 ± 0.11	+0.18	+0.04
10 May	−0.09	−0.05	−0.04	+0.00	0.16 (0.10)	+0.06 ± 0.06	+0.07	**−0.12**
20 May	−0.16	−0.08	−0.10	−0.02	0.12 (0.07)	−0.05 ± 0.10	**−0.12**	**−0.13**

* Larger value: Uncertainty from flux-divergence uncertainty assuming flux known at surface; smaller value assumes flux known at mid-boundary layer.

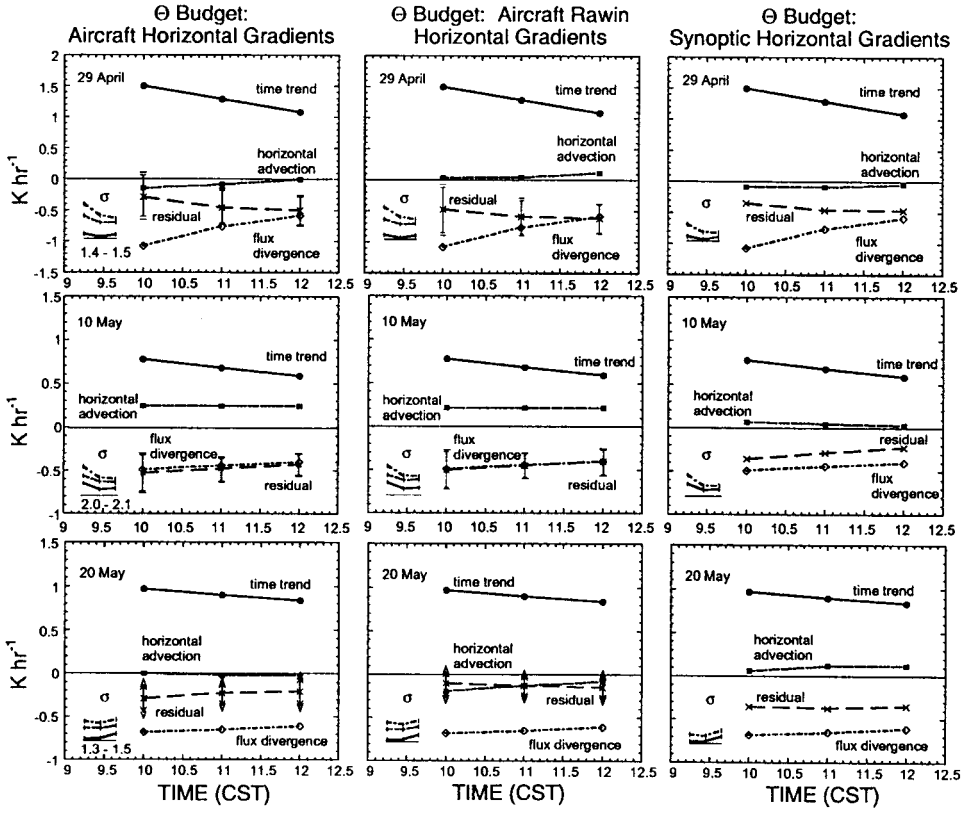

Figure 13. As in Figure 12, except (a) for mean mixed-layer potential temperature [Θ], (b) advection is also estimated using horizontal gradients from radiosondes and aircraft (middle column), and (c) estimated errors are plotted for all three times, according to the following convention: For time tendency: Difference between solid line and base of plot; for advection: Difference between short-dash and solid line; flux divergence: Difference between dot-dash and short-dash line.

TABLE VI
Impact of corrections on residual in Θ-budget (K hr^{-1}).

	Advection with ∇[Θ] from synoptic maps				Advection with ∇[Θ] from aircraft			
	Residual Figure 13	+A/C bias	+A/C +sfc bias	+AC +sfc bias +radiative warming*	Residual Figure 13	+A/C bias	+A/C +sfc bias	+A/C +sfc bias +radiative warming*
29 Apr	−0.45	−0.34	−0.27	−0.17	−0.45	−0.34	−0.27	−0.17
10 May	−0.29	−0.22	−0.20	−0.10	−0.48	−0.41	−0.39	−0.29
20 May	−0.37	−0.27	−0.21	−0.11	−0.23	−0.13	−0.07	+0.03

* Assumed ≈0.1 K hr^{-1}. There could be more direct heating by radiative flux divergence on 29 April and 10 May and less on 20 May (see text).

In all cases, the morning warming decreases with time, mainly in response to a vertical flux divergence whose magnitude decreases with time. Both trends reflect an increase in h: flux divergence and heating is 'diluted' as it is spread through the deepening mixed layer. Consistent with this, the day with the deepest mixed layer (May 10) warms most slowly, in spite of intermediate surface heat fluxes.

Horizontal advection based on all three gradient estimates is small for 29 April and 20 May. On 10 May, advection for all three estimates of ∇[Θ] indicates cooling, even though winds are from the south. Gradients based on aircraft and aircraft plus sondes both produce cold-air advection of 0.2–0.3 K hr^{-1}, while the gradients from synoptic maps produce a much smaller value (less than 0.1 K hr^{-1}).

5.3. Potential Causes of Θ-Budget Imbalance

The residual in the Θ-budget is negative for all three days, regardless of the method of estimating horizontal advection: *The estimated flux divergence and advection cannot account for the observed warming*. We discuss four potential sources of this systematic discrepancy: Aircraft biases in $\overline{w'\theta'}$, surface-flux tower biases in $\overline{w'\theta'}$, radiative flux divergence, and mesoscale circulations.

5.3.1. *Aircraft Biases*

In Section 4.2, we noted a 30% difference in $\overline{w'\theta'}$ for the two aircraft. Since the Twin Otter $\overline{w'\theta'}$ fluxes extrapolate to the surface value (normalised flux close to unity), it is reasonable to suggest that the average of the flux divergences obtained from both aircraft might be low by about 15 per cent. Applying this correction to the flux divergences reduces the residual by about 0.1 K hr^{-1} (Table VI).

TABLE VII

Boundary-layer warming (K hr^{-1}) by radiative flux divergence for sounding times.

Date/Time (CST)	Clear air*	Aerosol warming for selected visibilities**		
		16 km	32 km	48 km
29 Apr 0930	0.007	0.13	0.06	0.04
29 Apr 1100	0.025	0.17	0.09	0.07
29 Apr 1230	0.027	0.18	0.10	0.07
10 May 0930	−0.003	0.12	0.05	0.03
10 May 1100	0.017	0.16	0.09	0.06
10 May 1230	0.022	0.18	0.09	0.07
20 May 0930	0.013	0.14	0.07	0.05
20 May 1100	0.027	0.18	0.11	0.07
20 May 1230	0.03	0.19	0.11	0.08

* Fu and Liou (1993), average of heating computed from BEA, OXF, and WHI soundings.
** McKeen algorithm in Angevine et al. (1998b).

5.3.2. *Surface-Flux Biases*

As noted in Section 2.2.4, the ratio of $H+LE$ to net radiation minus soil heating is 0.91, 0.94, for 29 April and 10 May, and we estimate a value of 0.9 for 20 May. We assume that H (and thus $\overline{w'\theta'}$) is too low by the same fraction as $H + LE$. From Section 4.2.2, the vertical flux divergence is mainly derived from aircraft data. Thus we estimate the contribution of potential $\overline{w'\theta'}$ biases by adding the deficits (9% and 6%) to the aircraft-bias correction for 29 April and 10 May, and assume a 10% deficit for 20 May, reducing the residual further by between 0.02 and 0.07 K hr^{-1} (Table VI).

5.3.3. *Radiative Flux Divergence*

For the three days, Figure 14 shows the clear-air radiative heating rate from the surface to 700 hPa from the 1100 CST Beaumont soundings; and Table VII shows the average mixed-layer warming for clear air, and estimates of additional warming by aerosols for selected visibilities (Section 4.2.4). In general, the clear-air boundary-layer radiative flux divergences produce a net warming, of the order of 0.02–0.05 K hr^{-1}, similar to the hypothetical value quoted in Barr and Betts (1997) for spring/summer conditions over Canada's boreal forest. As noted in Section 4.2.4, the visibility is best on 20 May, with poorer visibility on 29 April and 10 May.

The numbers in the table suggest that 0.1 K hr^{-1} heating is plausible on any of the three days, consistent with Angevine et al. (1998b) and Angevine (1999). Adding this warming to the corrections for biases in aircraft and surface fluxes

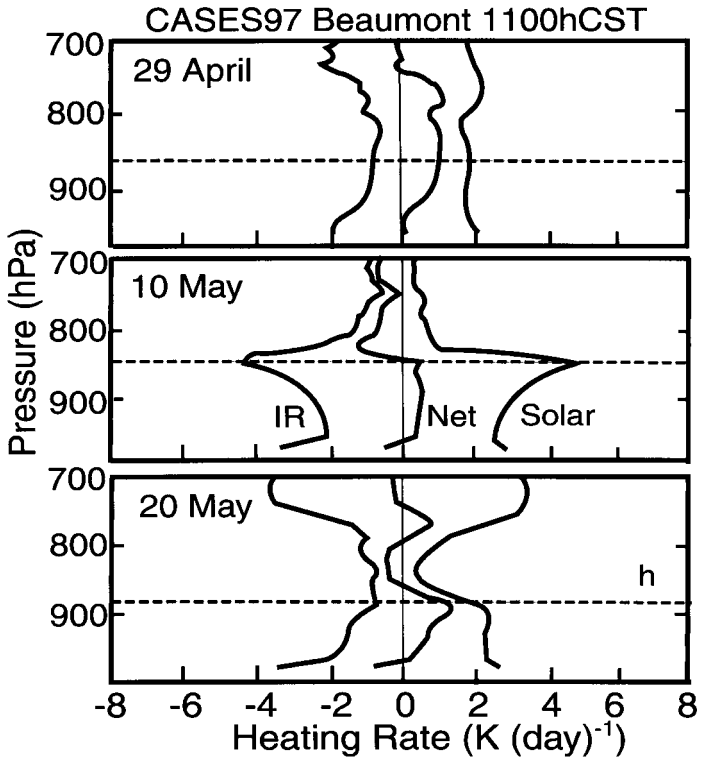

Figure 14. Solar, infrared, and net radiative heating of the mixed layer at Beaumont for clear air at 1100 CST, for the three days, using the Fu-Liou (1993) radiative transfer model. Dashed line shows mean depth of boundary layer at time of sounding.

(Table VI) brings all the budgets into balance to within the uncertainty of the calculations, with the notable exception of 10 May with horizontal advection using aircraft-derived $\nabla[\Theta]$ (and, from Figure 13, for $\nabla[\Theta]$ from aircraft and sondes). This residual would be smaller if the horizontal advection were smaller. In the following section, we present evidence that mesoscale circulations led to an overestimate of $\nabla[\Theta]$ and hence the advection term.

5.3.4. *Mesoscale Circulations*

Figure 15 illustrates the θ pattern for King Air mid-morning stacks for all three days. There is considerable horizontal variability on scales $>$ 10 km on both 29 April and 10 May, while the subsynoptic variability on 20 May is on scales $<$ 5 km. The Θ pattern on 29 April varied through the morning; and the along-wind component of $\nabla[\Theta]$ based on time-smoothed radiosonde and aircraft data was fortuitously similar to that from synoptic maps, leading to similar horizontal advection estimates in Figure 13. (Figure A2 shows that mesoscale variability did affect Θ gradients in the cross-wind direction, with different flux-leg and triangle-pattern values.) However, the aircraft and aircraft-plus-sondes estimates of $\nabla[\Theta]$ along the

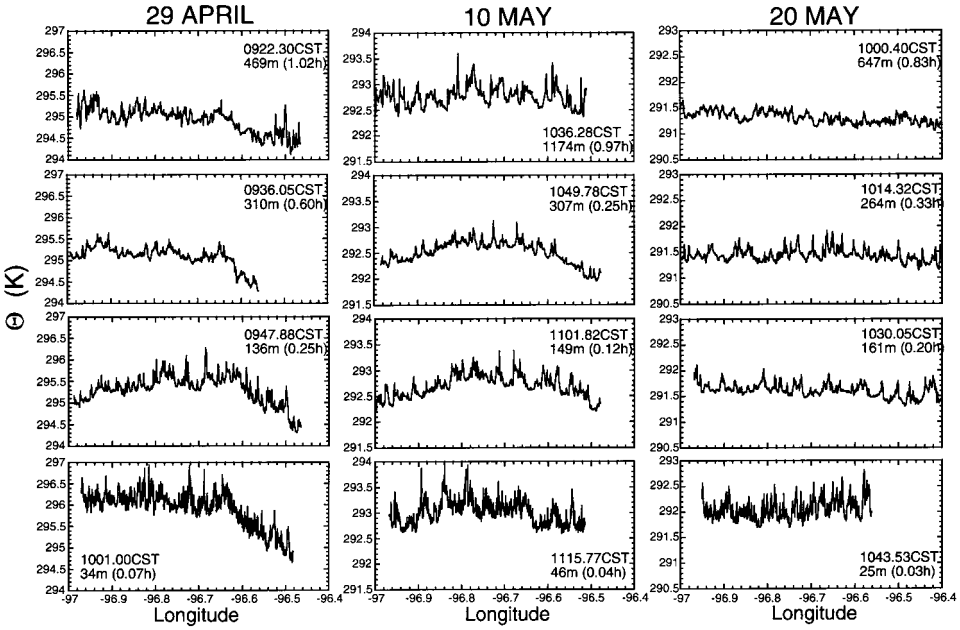

Figure 15. For King-Air mid-morning stacks, potential temperature along the southernmost track in Fig. 2 for 10 May and 29 April; and for the track just north of BEA for 20 May. For southern leg, 0.1° longitude equals 8.8 km, or about 9.7 km along the leg. For the northern (BEA) leg, 0.1° equals 8.8 km in the east–west direction and 8.9 km along the leg. Labels: Leg beginning time (CST) and height (m agl and normalized by h).

wind differed significantly from the synoptic estimates on 10 May. The persistence of the Θ pattern through the morning enables a closer look at its structure and impact. In this section, we (a) describe the mesoscale circulations associated with the Θ pattern, (b) show that the effect of the circulation on vertical fluxes should be small, and (c) show that error in $\nabla[\Theta]$ resulting from using sondes or aircraft triangle legs leads to a significant overestimate of cooling by advection.

Description of Mesoscale Circulation. The mesoscale θ maximum of 10 May is associated with convergence of the along-track (WSW-ENE) component of the wind $\partial u_s/\partial s$ in the lower mixed layer, and divergence in the upper mixed layer, suggesting that the circulation is mainly confined to the mixed layer. Figure 16 shows the vertical $\partial u_s/\partial s$ profile at 1100 CST, found by applying the time-trend technique to 16 King-Air flux legs. The vertical consistency in $\partial u_s/\partial s$ in the lower half of the mixed layer is remarkable, since the values were determined for different layers (L, M_1, and M_2 in Figure 7). Radar wind profiler-derived vertically-averaged components of the convergence over the watershed are shown for comparison. Note that $[\partial u_s/\partial s]$ ($\approx [\partial u/\partial x]$) over the watershed changes from near zero at 1030 CST to positive, consistent with the strong mixed-layer divergence that develops on this day. Coulter (1999) obtains an average subsidence of 30 mm s^{-1} at the top of the mixed layer during the daylight hours using both the minisodars and the radar wind

profilers, and radiosonde data revealed moisture features sinking at a rate of about 20 mm s^{-1} during the day.

In Figure 17, the radar wind profiler winds at the edges of the watershed suggest a watershed-scale boundary-layer circulation in the east-west direction. There is a divergence-convergence couplet in U at 1030 CST with divergence in the lower part of the mixed layer, and convergence above; the couplet is superimposed on divergence through the mixed layer at 1130 CST. The north-south components indicate roughly constant divergence through the mixed layer at both times, suggesting that the mesoscale circulations are mainly in the east-west direction. Note that the convergence and θ maximum are centred around 96.75° W, the highest terrain along the flight track (Figure 2). For comparison, the average aircraft winds measured in the stack pattern did not change with height, consistent with the assumption in deriving (1b).

From the forgoing discussion, Figures 16 and 17 suggest mixed-layer subsidence over the watershed and mixed-layer upwelling over the broad, relatively high terrain on the east side, supported mainly by convergence in the east-west or ENE-WSW direction, as pictured in Figure 18. Figure 16a shows the estimated vertical velocity in the mid-boundary layer based on the continuity equation, and the assumptions that (a) the convergence pattern is represented by the dashed line and (b) the convergence in the north-south direction does not contribute to *mesoscale* vertical velocity; i.e., the mesoscale circulation is approximately two-dimensional.

Effect on Vertical Flux Divergence. Under these assumptions, we can make a crude estimate of the mesoscale flux $\overline{w_m\theta_m}$. From Figure 16, $w(\partial u_s/\partial s)$ reaches a maximum of 0.015 m s^{-1} at $h/2$. If the flux legs sampled half a wavelength, this implies a mesoscale vertical velocity amplitude about twice that, or 0.03 m s^{-1}. From plots like Figure 15, the amplitude of the θ_m oscillation is about 0.2 K. Assuming sinusoidal variation and averaging over one wavelength, $\overline{w_m\theta_m} \approx 0.02$ K m s^{-1} at $h/2$, decreasing above and below. It is interesting but not conclusive that the quadratic fits to the θ-flux profiles for the two days with mesoscale variability show bulges at $h/2$, while that for 20 May does not. (20 mm s^{-1} vertical velocities at 10-km scales are within the noise for aircraft measurements, e.g., Lenschow, 1972 and Mahrt, 1998). Such a flux would contribute to a 0.14 K hr^{-1} cooling of the lower mixed layer and a corresponding heating of the upper mixed layer, with no net heating through the mixed layer.

The effect of the mesoscale eddies on entrainment is unknown. Peter Sullivan, Ned Patton, and Chin-Hoh Moeng (personal communication, 2001) simulated mesoscale eddies in a large-eddy simulation coupled to an LSM with spatially-varying soil moisture and thermodynamic conditions similar to those of CASES-97 and found a *decrease* in entrainment, but it is premature to generalise to other situations.

Horizontal Advection. From Figure 15, θ variability is on a scale comparable to the flux-leg length, making Θ-gradient estimates highly uncertain unless the variability is regular, steady, and the complete circulation is sampled. The association

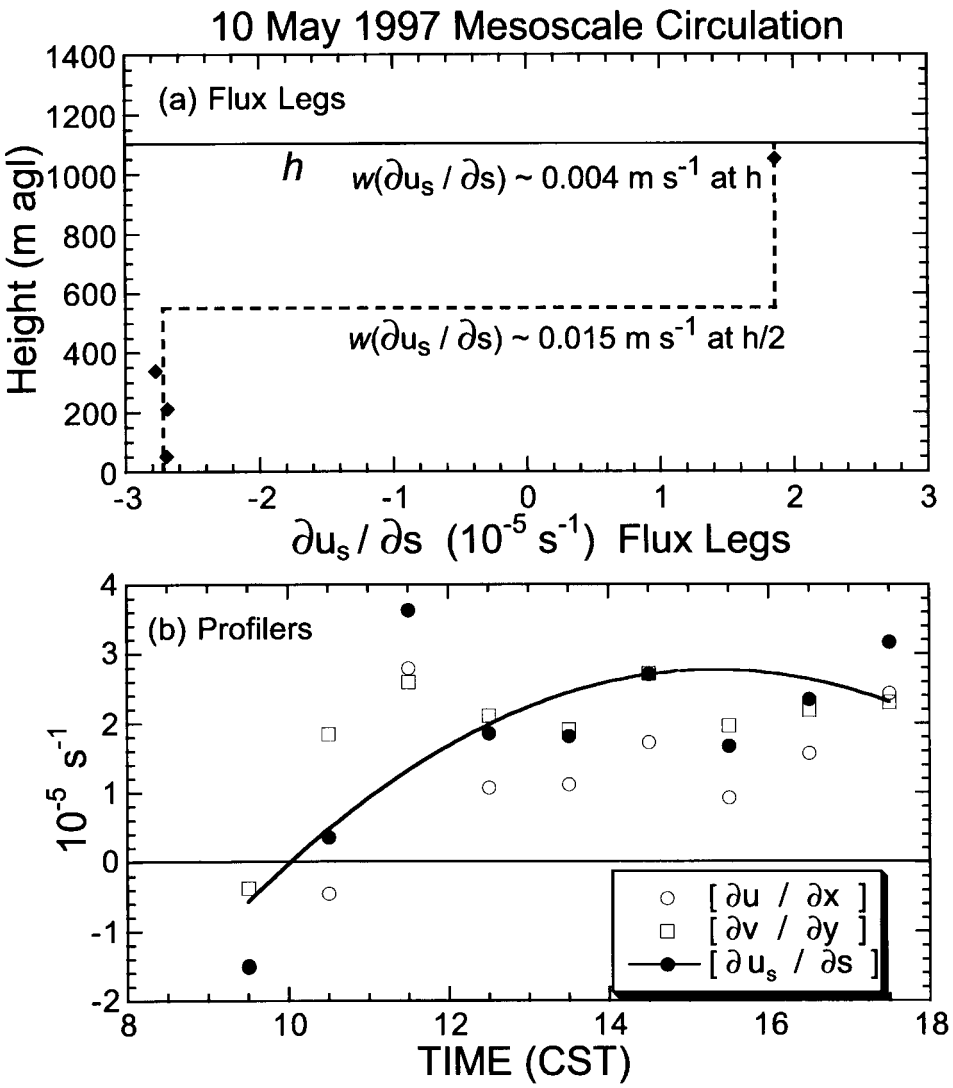

Figure 16. For 10 May, (a) convergence of wind component along the flux-stack track direction as a function of height at 1100 CST based on flux stacks using the time-trend technique, with $w(\partial u_s/\partial s)$ the vertical velocity computed from the along-track convergence assuming the dashed convergence profile. Uncertainty in aircraft $\partial u_s/\partial s$ is ≈30%, based on Lenschow et al. (1980). (b) Vertically-averaged convergence along the x (zonal), y (meridional), and s (flux-stack) directions over the Walnut River Watershed, estimated from the Beaumont–Whitewater–Oxford radar wind profiler triangle. Solid curve is quadratic least-squares best-fit line to $[\partial u_s/\partial s]$.

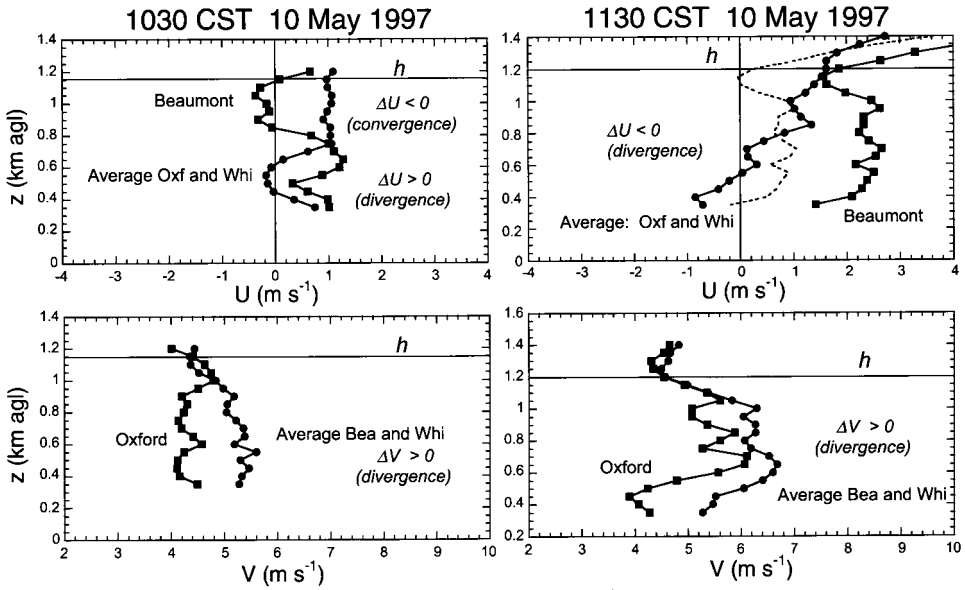

Figure 17. Comparison of u at the eastern (BEA) to average from western (OXF and WHI) profilers, and of v at the southern (OXF) to average from northern (BEA, WHI) profilers, as a crude indication of the mixed-layer divergence pattern over the watershed. Dash line for u at 1130 CST: u(Beaumont) offset by 1.6 m s^{-1} to highlight convergence–divergence pattern superposed on strong subsidence.

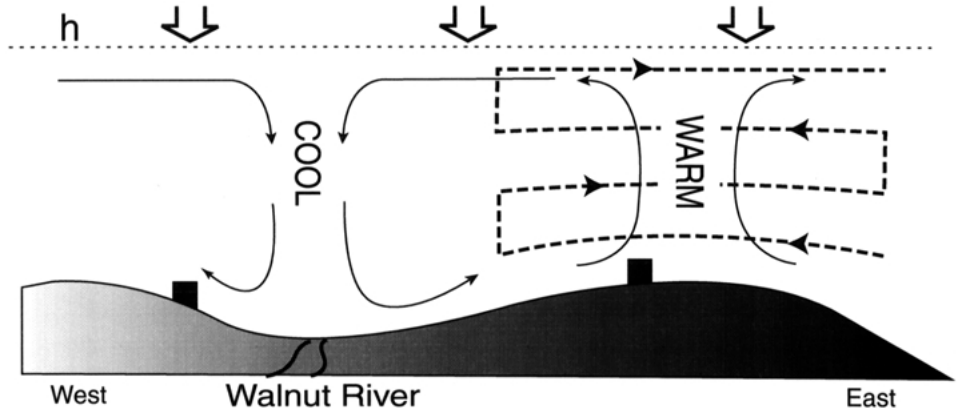

Figure 18. Schematic west–east cross section of mesoscale circulation on 10 May. Thin arrows denote mesoscale motions; large open arrows denote synoptic-scale subsidence, which extends into the mixed layer. Dashed lines are schematic flux legs; squares are approximate average position of Whitewater and Oxford, and position of Beaumont relative to the watershed. Dotted line is schematic average top of mixed layer.

of higher temperatures with higher elevations suggests that the north-south temperature gradient on 10 May is overestimated when one assumes linear variation along the sides of the BEA-WHI-OXF triangle or uses the sondes at the vertices, since the south vertex, Oxford, is at 360 m msl (cooler), and the two northern vertices, Beaumont and Whitewater, are above 400 m (warmer, Figure 2). With a south wind, this results in artificially large cooling. Indeed, the afternoon triangle legs have a mesoscale θ minimum over the middle of the watershed on the BEA-WHI leg (Figures 2, 19) – a clear violation of the linearity assumption. Estimating a gradient from Θ at Oxford to the θ average for the BEA-WHI flight track, would thus produce a better estimate of the horizontal advection, probably closer to the synoptic estimate but still slightly large, since the average elevation is higher to the north. Had we adequate data to calculate the watershed-scale gradient accurately, we suspect it would produce horizontal advection close to the synoptic value and balance the 10 May budget.

The inconsistency between a significantly overestimated north-south Θ gradient and the good agreement between gradients observed on ENE-WSW flux legs (Figure 2) and gradients along the same heading predicted from triangle legs (Section 4.2.3, Appendix A, Figure A2) is related to the orientation of the flux legs and is fortuitous. *The failure of straightforward comparisons and scatter in identifying the problem in the north-south gradients underscores the importance of rigorous error analysis and careful examination of the data used in gradient estimations.*

Causes of Mesoscale Circulations. The association of near-surface divergence with low terrain and near-surface convergence with warm, high terrain is consistent with the pattern discussed by Shaw and Doran (2001). The vegetation may play a role as well. Land-use maps of the region indicate a minimum of 70-km fetch (about 4 h for air travelling at 5 m s^{-1}) over grass for the warm air, and over mixed crops and grass for the cool air, before reaching the latitude where the mesoscale circulations were documented by the King Air. Using a combined modelling and observational study, Segal et al. (1989) also concluded that land use and terrain both influence mesoscale variability. Actual observations of land-use generated circulations are rare. Mahrt et al. (1994) found weak 'inland breezes', during light-wind situations in the extremely flat terrain of California's Central valley, but only at 33 m. Bougeault et al. (1991), Mahrt and Ek (1993) and others report evidence of 'forest breezes' in HAPEX (Andre et al., 1988), again on a day with light winds.

The observed circulations are smaller horizontally than those often associated with idealised land-surface variability. For example, when Avissar and Chen (1993) and Chen and Avissar (1994) doubled the widths of alternating strips of wet and dry ground from 40 km to 320 km in a series of model runs, the strongest circulations that developed were 160 km across (80 km strips), consistent with the local Rossby deformation radius, as predicted by Dalu et al. (1991).

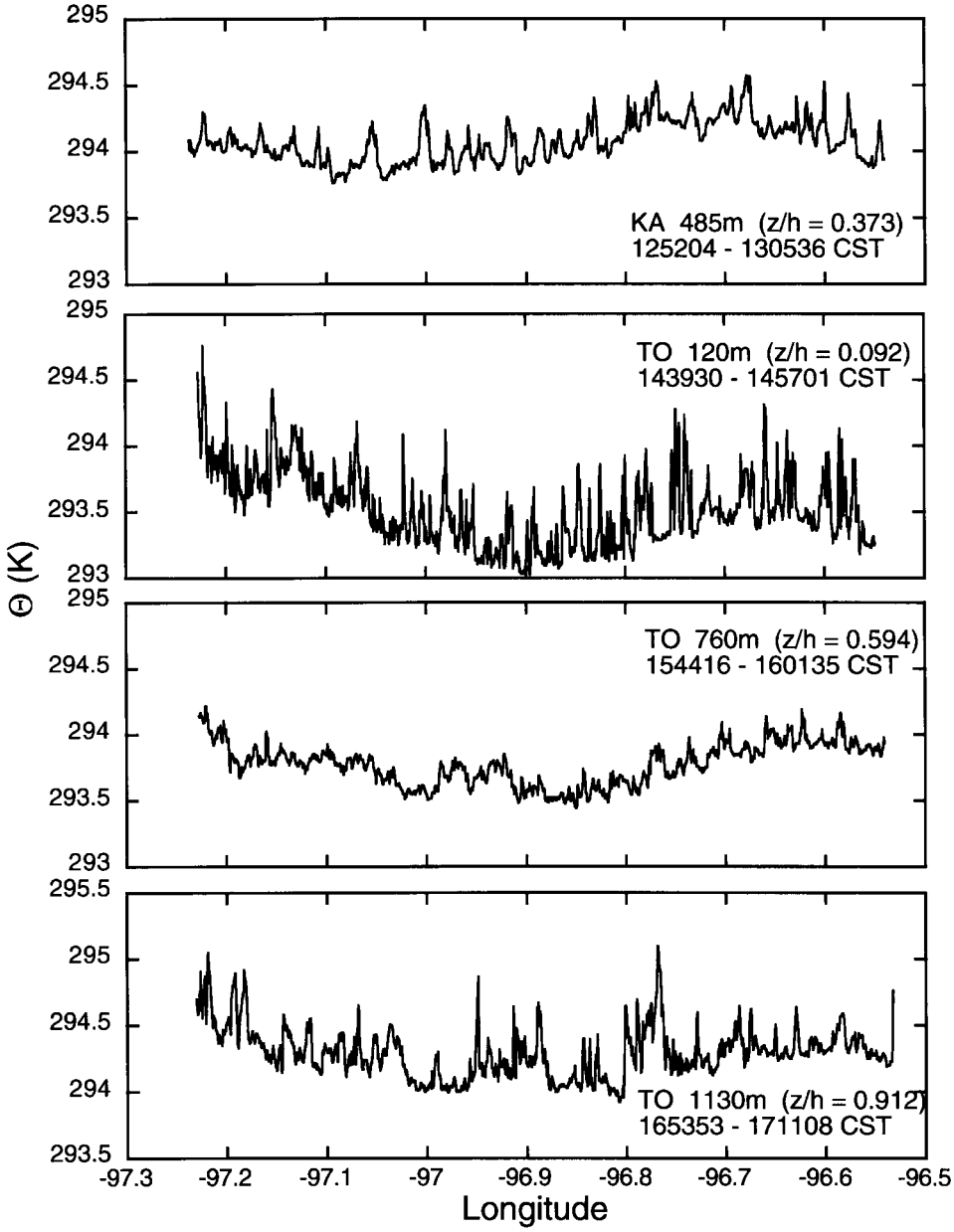

Figure 19. Potential temperature θ along Beaumont–Whitewater leg as a function of longitude. For terrain elevations along this leg, see Figure 2.

6. Conclusions

The computation of the $[\Theta]$ and $[Q]$ budgets for the late morning on three separate days spanning CASES-97 (Figures 12, 13) reveals that vertical flux divergence explains only part of the evolution. On 29 April, which has the strongest southerly winds, moistening by horizontal advection using both aircraft and synoptic values of $\nabla[Q]$ is significant. This is not a surprise: Northward transport of Gulf of Mexico moisture is a well-known precursor to precipitation in the midwest of the U.S.A. Consistent with the much larger diurnal variability in temperature, the vertical turbulence flux divergence dominates the morning warming. Smaller but potentially significant is direct mixed-layer warming from solar radiation: with aerosols due to agricultural burning, the warming could be as large as 0.1 K hr^{-1}. Heating/cooling from advection based on synoptic gradients is comparable.

The differences between the budgets for the three days are a function of mixed-layer depth, wind direction, and surface heterogeneity. Figure 12 shows that vertical flux divergence at 1100 CST had a moistening effect on 20 May, the day with saturated soil and green vegetation, and a drying effect on the other two days; but the large uncertainties indicate these results should be interpreted with caution. $[Q]$ increased most slowly on 29 April, in spite of apparent moist advection in both synoptic and mesoscale data, consistent with large vertical flux divergence, dry ground, and dormant vegetation. Morning mixed-layer warming was most rapid for 29 April, due to the largest surface fluxes (Figure 3) and a shallow mixed layer (Figure 5). Warming was slowest for 10 May (high soil moisture contrast, intermediate vegetation contrast), in spite of intermediate surface heat fluxes, because the mixed layer was the deepest. Surface heterogeneity is associated with both mesoscale mixed-layer variability and greater budget uncertainties.

As for previous budget calculations, there is significant uncertainty. However, some additional results emerge:

- The Q-budgets at 1100 CST are balanced within the large uncertainty of the terms for two of the three days; for the third day, balance occurs for advection using $\nabla[Q]$ from aircraft.
- On all three days, vertical flux divergence, advection, and radiative flux divergence are apparently not sufficient to account for the morning mixed-layer warming if error bars in Figure 13 are valid. However, allowing for possible biases in aircraft fluxes and surface fluxes, and accounting for $\approx$ 0.1K hr^{-1} heating from radiative flux divergence balances all the Θ-budgets at 1100 CST except for those for May 10 with horizontal advection based on aircraft-derived or aircraft-plus-sonde derived $\nabla[\Theta]$.
- There was significant mesoscale (10–100 km) θ variability on 29 April and 10 May, both days with heterogeneous surface properties and southerly winds. For 10 May, the θ pattern persisted through the morning, and aircraft- and profiler-derived divergences and aircraft θ measurements suggest the mesoscale circulation depicted in Figure 18. As shown in the figure, the circulation is tied to the terrain,

consistent with the results of Shaw and Doran (2001), but surface fluxes could play a role as well. The synoptic maps suggest a slight advective cooling, with south winds and a positive south-north temperature gradient. However, $\nabla[\Theta]$ based on aircraft or aircraft and sondes appears to be too large and leads to unrealistically large advective cooling. The erroneously large south-north $[\Theta]$ gradients are due to the association of higher Θ with higher terrain: Oxford, at the southern tip of the WHI-OXF-BEA triangle, is coolest because it is at the lowest elevation. Further, the minimum in Θ over the lower terrain beneath the BEA-WHI leg of the triangle (Figures 2, 19) is not accounted for when gradients are computed from soundings at the triangle vertices or from along-leg linear trends computed from aircraft legs connecting the vertices. *If a correction for advection error could be added to corrections for flux biases and radiative heating, the budget would probably balance on 10 May for aircraft- and aircraft-plus sondes* $\nabla[\Theta]$ *estimates.*

Considerable effort was necessary to minimise uncertainty in the budgets. Since the budgets are for late morning, when Θ and Q were evolving rapidly, we corrected fluxes and leg means for time trends before computing gradients. Flux values were adjusted to common times using objectively-determined time trends at corresponding levels or through normalisation with surface values, before computing the vertical flux divergence. The vertical flux divergences derived from the various methods were then averaged. For horizontal advection, horizontal gradients were found using aircraft tracks around the ≈60-km BEA-OXF-WHI profiler triangle after correction for time trends, or from radiosondes released at the three vertices in combination with the aircraft gradients. Error analysis led us to conclude that:

- Typical uncertainties were 0.05–0.1 K $hr^{-1}$for $\partial[\Theta]/\partial t$ and 0.03–0.1 g kg^{-1} hr^{-1} for $\partial[Q]/\partial t$.
- Using integral scales from Lenschow and Stankov (1986) in Mann and Lenschow (1995), flux-divergence uncertainty was 0.05–0.10 K hr^{-1} for θ using pairs of stacks, and $0.03 - 0.07$ g $kg^{-1}hr^{-1}$ for q using data from the whole morning. Estimating integral scales from the King Air data increased these uncertainties by a factor of 1.5 to 2 for Θ and a factor of about 1.5 for Q, with surface heterogeneity associated with higher values. Using changes in Θ and Q across the entrainment layer reduced residuals in the Q-budget on 10 and 20 May. However, except for 20 May, uncertainties are as large or larger than those for flux divergence calculated directly; and errors associated with the choice of z_i are not included in the estimates of uncertainty.
- The typical uncertainties for aircraft triangle patterns computed from Lenschow et al. (1980) and with integral scale $l_\Psi \approx h$, were ≈0.34 K $(100\ km)^{-1}$ for $\nabla[\Theta]$, and ≈0.33 g $kg^{-1}(100\ km)^{-1}$ for $\nabla[Q]$, about a third of the observed gradients. Actual $\nabla[\Theta]$ uncertainties in the budgets for 29 April and 10 May were 2–3 times as large, because they were based on extrapolation of the best-fit line through the triangle patterns, which were flown after the budget times. Even though $\nabla[Q]$ was also extrapolated, smaller scatter about the best-fit line led to uncertainties comparable to the typical values. With wind-component uncertainty of the

order of 0.5 m s^{-1}, the resulting uncertainties in advection are 0.1–0.25 K hr^{-1} for θ and 0.07–0.2 g $kg^{-1}hr^{-1}$ for Q. However, while $l_\Psi \approx h$ on 20 May validating the estimated uncertainties, *mesoscale variability on the other two days leads to unknown uncertainties, in spite of reasonable agreement in horizontal gradients along the same heading for flux and triangle legs.*

• Synoptic maps appear to produce reasonable values of horizontal gradients for estimates of horizontal advection.

•The uncertainty in the radiative flux divergence term is mainly due to uncertainty of the effects of aerosols. Deviations in the solar and infrared heating profiles produced by perturbed temperature and humidity profiles with the sonde errors described above are within 5%.

Acknowledgements

The authors gratefully acknowledge the several people without whose help this paper would not have been possible. Don Lenschow, Jielun Sun and two anonymous reviewers who reviewed the paper and made several useful suggestions. Steve Oncley coordinated NCAR's support from the planning stages through the data correction and analysis; and Ned Chamberlain and Larry Murphy kept the balloon launches going during CASES-97. Oncley and others from NCAR's SSSF set up and maintained the 8 PAM III stations. Glenn Gordon and his co-workers of NSF's University of Wyoming flight facility kept the King Air operations running smoothly. Argonne National Laboratory set up the ABLE network in time for the experiment, and made the data available in real time, an invaluable aid in guiding aircraft patterns. We also acknowledge the scientific and operational crews for the NOAA Twin for their support. The Twin Otter and its crews, and the surface tower at site 10, were supported entirely by NOAA's Air Resources Laboratory. Jerry Klazura (Argonne) and Julie Lundquist (University of Colorado) helped in all phases of the experiment and made the CASES-97 Operations Center a fun and stimulating place to be. The landowners who allowed us to set out our instruments were gracious hosts, and connected us to the community. The King Air, radiosondes, and eight surface flux stations were provided through the NSF deployment pool; NOAA ATDD provided the ninth tower used in this paper. One of us (ML) spent part of her sabbatical with SM and WA in Susan Solomon's group at the NOAA Aeronomy Lab working on this paper; their help and hospitality is gratefully acknowledged. RLG, Co-PI with ML was supported by NSF Grant ATM-9615583. FC was partially supported by NASA Research Grant NAG-5-7541 and the Land Surface Hydrology Program in the Office of Earth Sciences.

Appendix A

A.1. Error in estimating the horizontal gradient

To estimate the error in the horizontal gradient based on Ψ estimates at the vertices of the Beaumont–Oxford–Whitewater triangle, we start with the solution of (3),

$$\frac{\partial \Psi}{\partial x} = \frac{1}{D}\left(sin\phi_2\left(\frac{\partial \Psi}{\partial s_1}\right) - sin\phi_1\left(\frac{\partial \Psi}{\partial s_2}\right)\right)$$

$$\frac{\partial \Psi}{\partial y} = \frac{1}{D}\left(cos\phi_1\left(\frac{\partial \Psi}{\partial s_2}\right) - cos\phi_2\left(\frac{\partial \Psi}{\partial s_1}\right)\right), \tag{A1}$$

where

$$D = cos\phi_1 sin\phi_2 - cos\phi_2 sin\phi_1. \tag{A2}$$

We assume that the errors in estimating ϕ_1 and ϕ_2 are negligible, and that the errors in the gradients along the sides of the triangle are equal in magnitude. Thus

$$|\epsilon_{\partial\Psi/\partial s1}| = |\epsilon_{\partial\Psi/\partial s2}| = |\epsilon_{\partial\Psi/\partial s}|. \tag{A3}$$

We replace each gradient by the sum of the true gradient and an uncertainty, i.e.,

$$\left(\frac{\partial \Psi}{\partial x_i}\right) = \left(\frac{\partial \Psi}{\partial x_i}\right)_0 \pm \epsilon_{(\partial\Psi/\partial x_i)}, \tag{A4}$$

where $\epsilon_{(\partial\psi/\partial x_i)} \geq 0$ and x_i represents s_1, s_2, x, and y. Substituting (A4) into (A1) and applying (A3),

$$\left(\frac{\partial \Psi}{\partial x}\right)_0 \pm \epsilon_{\partial\Psi/\partial x}$$

$$= \frac{1}{D}\left[\sin\phi_2\left(\frac{\partial \Psi}{\partial s_1}\right)_0 \pm \sin\phi_2\epsilon_{\partial\Psi/\partial s} - \sin\phi_1\left(\frac{\partial \Psi}{\partial s_2}\right)_0 \pm \sin\phi_1\epsilon_{\partial\Psi/\partial s}\right],$$

$$\left(\frac{\partial \Psi}{\partial y}\right)_0 \pm \epsilon_{\partial\Psi/\partial y}$$

$$= \frac{1}{D}\left[\cos\phi_1\left(\frac{\partial \Psi}{\partial s_2}\right)_0 \pm \cos\phi_1\epsilon_{\partial\Psi/\partial s} - \cos\phi_2\left(\frac{\partial \Psi}{\partial s_1}\right)_0 \pm \cos\phi_2\epsilon_{\partial\Psi/\partial s}\right]. \tag{A5}$$

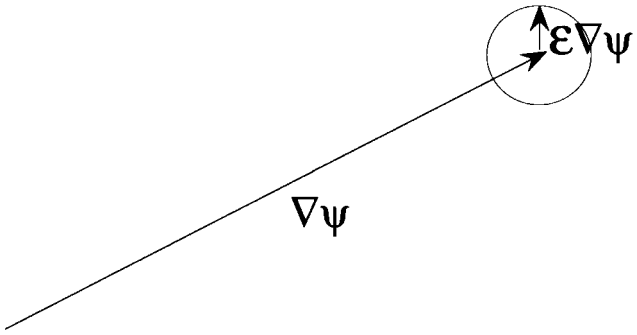

Figure A1. Illustration of the error in horizontal gradient $\epsilon_{\nabla\Psi}$ as it relates to the gradient $\nabla\Psi$.

Subtracting out (A1) and rearranging:

$$\epsilon_{\partial\Psi/\partial x} = \frac{1}{D}\epsilon_{\partial\Psi/\partial s}(|\sin\phi_2| + |\sin\phi_1|)$$

$$\epsilon_{\partial\Psi/\partial y} = \frac{1}{D}\epsilon_{\partial\Psi/\partial s}(|\cos\phi_2| + |\cos\phi_1|), \tag{A6}$$

where absolute values are added to maximise the estimated error. The magnitude of the vector gradient error is:

$$\epsilon_{\nabla\Psi} = \frac{1}{D}\epsilon_{\partial\Psi/\partial s}\left[(|\sin\phi_2| + |\sin\phi_1|)^2 + (|\cos\phi_2| + |\cos\phi_1|)^2\right]^{\frac{1}{2}}. \tag{A7}$$

The gradient error can be in any direction (Figure A1).

To obtain the error magnitude in estimating the horizontal gradient for radiosondes released simultaneously from Beaumont, Oxford, and Whitewater, we set $\phi_1 = 0°$ and $\phi_2 = 60°$ in (A7),

$$\epsilon_{\nabla\Psi(r\triangle)} = 2\epsilon_{\partial\Psi/\partial s}, \tag{A8}$$

where the $r\triangle$ denotes a radiosonde triangle.

To estimate the error for an aircraft triangle, we note that the best-fit line for each flight track provides a value of Ψ at the leg-end points. Thus the three triangle legs provide *two* Ψ values at each of the vertices. Since it takes three points to define a plane (or to solve (3) and (4)), the triangle patterns provide two independent samples of the gradient. Therefore the gradient uncertainty for a complete aircraft triangle ($a\triangle$) is:

$$\epsilon_{\nabla\Psi(a\triangle)} = 2^{\frac{1}{2}}\epsilon_{\partial\Psi/\partial s}. \tag{A9}$$

Typical gradient estimates are compared to the estimated uncertainty for aircraft- and radiosonde-derived gradients in Table AI. For the aircraft, $\epsilon_{\partial\Psi/\partial s}$ is

TABLE AI

Uncertainty estimates for horizontal gradients. Typical gradients are $\nabla\Theta = 1$ K (100 km)$^{-1}$ and $\nabla Q = 1$ g kg^{-1} (100 km)$^{-1}$. Gradient uncertainty units (K (100 km)$^{-1}$ for Θ, g kg^{-1} (100 km)$^{-1}$ for Q).

Variable	Aircraft			Sondes		
	$\varepsilon_{\partial\Psi/\partial s}$*	$\varepsilon_{\nabla\psi(a\Delta)}$	$\sigma_{\nabla\psi(a\Delta)}$**	ε (sonde)	$\varepsilon_{\nabla\psi(r\Delta)}$	$\varepsilon_{\nabla\psi(4r\Delta s)}$
Θ	0.24	0.34	0.36	0.20 K	1.33	0.65
				0.50 K	3.33	1.65
Q	0.23	0.33	0.15	0.3 g kg^{-1}	2.00	1.00
				0.8 g kg^{-1}	5.33	2.67

* Based on Lenschow et al. 1980 (see text).
** Standard deviation from best fit line to gradients vs. time.

the average of the uncertainties based on equation (A11) in Lenschow et al. (1980) with $l_x = h$, and triangle errors are found from our (A9). The third column shows standard deviations relative to the linear fit to the gradients derived from the three-to-four triangles flown on each day. The uncertainties are roughly 15–35% of the typical gradients.

Radiosonde gradient errors in Table AI are estimated from (A8). An 0.2 K sonde Θ uncertainty implies $\epsilon_{\partial\Theta/\partial s} = 0.4$ K/Δs, where the distance Δs between sondes is ≈60 km. Thus $\epsilon_{\nabla\Psi(r)} = 0.8$ K/$\Delta s = 1.33$ K (100 km) s^{-1} for a set of three sondes released simultaneously from Beaumont, Oxford, and Whitewater. Using four sets of three sondes, the expected gradient error is reduced by half, making the resulting uncertainty about twice that for one aircraft triangle. This relatively large uncertainty led to use of a minimum of four sets of sondes for determination of Θ gradients. For mixing ratios, the expected error for four sets of sondes and a 2% humidity uncertainty is three times that for one aircraft triangle.

The interleaving of aircraft triangles, sonde releases, and flux legs in the afternoon offers an excellent opportunity to compare gradients from the three sources. Figure A2 shows the afternoon Θ and Q gradients found from radiosondes and aircraft triangles. The radiosonde humidity gradients have more scatter than the aircraft humidity gradients, but less scatter than might be expected from Table AI. Comparing the gradients along the flux-leg heading for the flux legs and from the triangles, agreement is best on 10 May and worst on 29 April. Bad agreement does not necessarily mean that either gradient estimate is wrong, since the gradients were computed over different locations (see Figure 2). However, good agreement provides no information about the quality of the gradients orthogonal to the flux-leg tracks (Section 5.3.4).

Since the triangles were flown in the afternoon, and the budgets were computed for the morning, extrapolation is required to obtain triangle-based gradients. Table AII shows the gradient uncertainties at budget times for 29 April and 10 May,

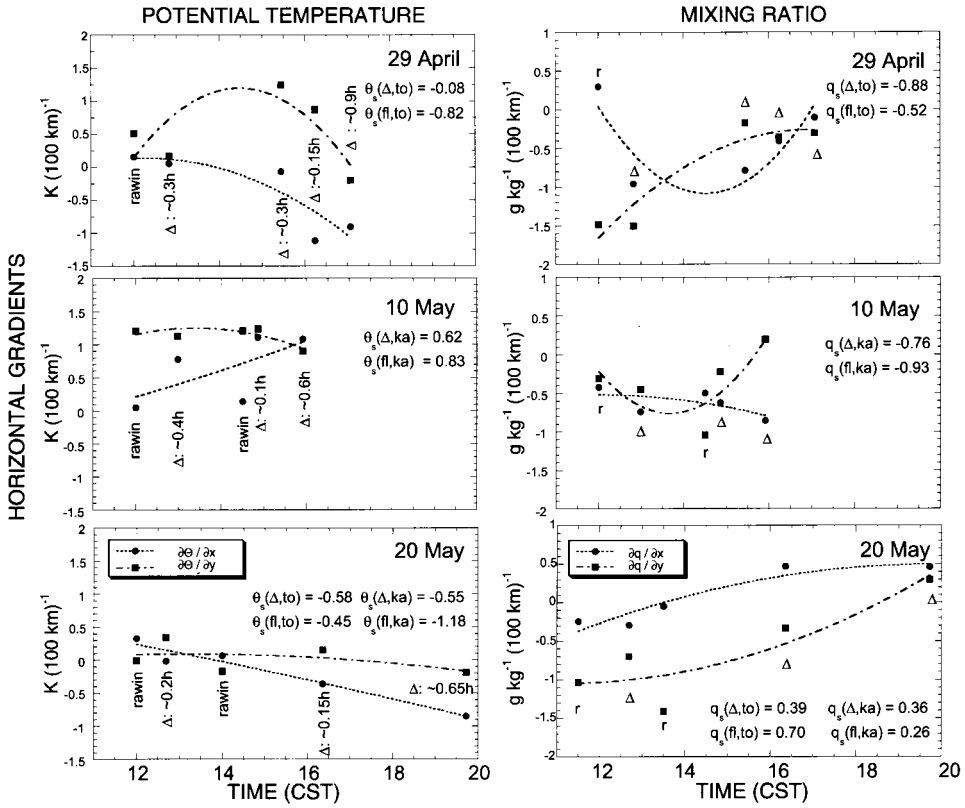

Figure A2. Comparison of horizontal gradients along x (zonal) and y (meridional) directions based on radiosonde and aircraft triangles for the three days. Numbers on the graphs are average flux-leg (fl) gradients, and the predicted gradient along the flux-leg heading, based on aircraft-triangle gradients interpolated to the average flux-leg time (triangle symbol). ka = King Air, to = Twin Otter.

TABLE AII

Gradient uncertainties (K (100 km)$^{-1}$ for Θ, g kg^{-1} (100 km)$^{-1}$ for Q), from extrapolation (worst-case) for 1000, 1100, and 1200 CST.

Date	Θ_x, Θ_y (10)	Θ_x, Θ_y (11)	Θ_x, Θ_y (12)	Q_x, Q_y (11)
29 Apr	0.98, 0.77	0.76, 0.60	0.55, 0.43	0.23, 0.31
10 May	0.18, 0.36	0.14, 0.28	0.10, 0.20	0.21, 0.20

based on (a) calculating the standard deviation with respect to the best-fit line to the triangle data (one point per triangle, 3-4 triangles), (b) defining a 'worst-case' new line by adding the standard deviation σ to $\partial\Psi_x/\partial x_i$ at one end of the best fit line,* and subtracting σ from $\partial\Psi_x/\partial x_i$ at the other end, and then (c) taking the difference between the Ψ_x values obtained from the new line and those obtained from the original best-fit line. On 20 May, we used the flux legs (flown parallel to the wind) and the first triangle to obtain the horizontal gradients.

References

Andre, C., Goutorbe, J.-P., Perrier, A., Becker, F., Bessemoulin, P., Bougeault, P., Brunet, Y., Brutsaert, W., Carlson, T., Cuenca, R., Gash, J., Gelpe, J., Hildebrand, P., Lagouarde, J. P., Lloyd, C., Mahrt, L., Mascart, P., Mazaudier, C., Noilhan, J., Ottle, C., Payan, M., Phulpin, T., Stull, R., Shuttleworth, J., Schmugge, T., Taconet, O., Tarrieu, C., Thepenier, R. M., Valancogne, C., Vidal-Madjar, D., and Weill, W.: 1988, 'Evaporation over Land-Surfaces: First Results from HAPEX-MOBILHY Special Observing Period', *Ann. Geophys.* **6**, 477–492.

Angevine, W. M.: 1999, 'Entrainment Results Including Advection and Case Studies from the Flatland Boundary Layer Experiments', *J. Geophys. Res.* **104**, 30,947–30,963.

Angevine, W. M. and MacPherson, J. I.: 1995, 'Comparison of Wind Profiler and Aircraft Wind Measurements at Chebogue Point, Nova Scotia', *J. Atmos. Oceanic Tech.* **12**, 421–426.

Angevine, W. M., Bakwin, P. S., and Davis, K. J.: 1998a, 'Wind Profiler and RASS Measurements Compared with Measurements from a 450-m-Tall Tower', *J. Atmos. Oceanic Tech.* **15**, 818–825.

Angevine, W. M., Grimsdell, A. W., McKeen, S. A., and Warnock, J. M.: 1998b, 'Entrainment Results from the Flatland Boundary Layer Experiments', *J. Geophys. Res.* **103**, 13,689–13,701.

Auble, D. R. and Meyers, T. M.: 1992, 'An H_2O and CO_2 Open Path Gas Analyzer for Use with Eddy Flux Systems', *Boundary-Layer Meteorol.* **59**, 243–256.

Avissar, R. and Chen, F.: 1993, 'Development and Analysis of Prognostic Equations for Mesoscale Kinetic Energy and Mesoscale (Subgrid-Scale) Fluxes for Large Scale Atmospheric Models', *J. Atmos. Sci.* **50**, 3751–3774.

Barr, A. G. and Betts, A. K.: 1997, 'Radiosonde Boundary Layer Budgets above a Boreal Forest', *J. Geophys. Res.* **102**, 29,205–29,212.

Betts, A. K.: 1992, 'FIFE Atmospheric Boundary Layer Budget Methods', *J. Geophys. Res.* **97**, 18,523–18,532.

Betts, A. K., Desjardins, R. L., MacPherson, J. I., and Kelly, R. D.: 1990, 'Boundary Layer Heat and Moisture Budgets from FIFE', *Boundary-Layer Meteorol.* **50**, 109–137.

Betts, A. K., Desjardins, R. L., and MacPherson, J. I.: 1992, 'Budget Analysis of the Boundary Layer Grid Flights during FIFE 1987', *J. Geophys. Res.* **97**(D17), 18,533–18,546.

Bougeault, P., Bret, B., Lacarrere, P., and Noilhan, J.: 1991, 'An Experiment with an Advanced Surface Parameterization in a Mesobeta-Scale Model. Part II: The 16 June 1986 Simulation', *Mon. Wea. Rev.* **119**, 2374–2392.

Brandes, E. A., Vivekanandan J., and Wilson, J. W.: 1999, 'A Comparison of Radar Reflectivity Estimates of Rainfall from Collocated Radars', *J. Atmos. Oceanic Technol.* **16**, 1264–1272.

Brown, E. N., Friehe, C. A., and Lenschow, D. H.: 1983, 'The Use of Pressure Fluctuations on the Nose of an Aircraft for Measuring Pressure Fluctuation', *J. Clim. Appl. Meteorol.* **22**, 171–180.

Chen, F. and Avissar, R.: 1994, 'The Impact of Land-Surface Wetness Heterogeneity on Mesoscale Heat Fluxes', *J. Appl. Meteorol.* **50**, 3751–3774.

* The end points of the lines are defined by the times of the first and last gradient estimates.

Chen, F., Mitchell, K., Schaake, J., Xue, Y., Pan, H., Koren, V., Duan, Y., Ek, M., and Betts, A.: 1996, 'Modeling of Land-Surface Evaporation by Four Schemes and Comparison with FIFE Observations', *J. Geophys. Res.* **101**, 7251–7268.

Coulter, R.: 1999, 'Convergence Estimates over the ABLE Region during CASES-97 Obtained from Radar Wind Profiler and Sodar Data', in *Preprints 13th Symposium on Boundary Layers and Turbulence*, American Meteorological Society, Dallas, 10–15 Jan., pp. 508–511.

Coulter, R. L. and Holdridge, D. H.: 1998, 'A Procedure for the Automatic Estimation of Mixed Layer Height', in *Proceedings of the 8th Atmospheric Radiation Measurement (ARM) Program Science Team Meeting*, Tucson, Department of Energy Office of Energy Researth, pp. 177–180.

Coulter, R., Klazura, J., Lesht, B. M., Shannon, J. D., Sisterson, D. L., and Wesely, M. L.: 1998, 'Using the ABLE Facility to Observe Urbanization Effects on Planetary Boundary Layer Processes', in *Proceedings 10th Joint Conference on the Applications of Air Pollution Meteorology*, American Meteorological Society, Air and Waste Management Association Joint Conference, Phoenix, AZ, 11–16 Jan, pp. J76–J79.

Crawford, T. L. and Dobosy, R. J.: 1992, 'A Sensitive, Fast-Response Probe to Measure Turbulence and Heat Flux from Any Airplane', *Boundary-Layer Meteorol.* **59**, 257–278.

Dalu, G. A., Pielke, R. A., Avissar, R., Kallos, G., Baldi, M., and Guerrini, A: 1991, 'Linear Impact of Thermal Inhomogeneities on Mesoscale Atmospheric Flux with Zero Synoptic Wind', *Ann. Geophys.* **9**, 641–647.

Eloranta, E. W. and Forrest, D. K.: 1992, 'Volume-Imaging Lidar Observations of the Convective Structure Surrounding the Flight Path of a Flux-Measuring Aircraft', *J. Geophys. Res.* **97**, 18,383–18,393.

Fitzjarrald, D. R., Acevedo, O. C., and Moore, K. E.: 2001, 'Climatic Consequences of Leaf Presence in the Eastern United States', *J. Climate* **14**, 598–614.

Freedman, J. M., Fitzjarrald, D. R., Moore, K. E., and Sakai, R. K.: 2001, 'Boundary Layer Clouds and Vegetation-Atmosphere Feedbacks', *J. Climate* **14**, 180–197.

Friehe, C. A. and Khelif, D.: 1993, 'Fast Response Aircraft Temperature Sensors', *J. Atmos. Oceanic Tech.* **9**, 784–795.

Fu, Q., and Liou, K. N.: 1993, 'Parameterization of the Radiative Properties of Cirrus Clouds', *J. Atmos. Sci.* **50**, 2008–2025.

Furger, Markus, Whiteman, C. D., and Wilczak, J. M., 1995, 'Uncertainty of Boundary Layer Heat Budget Computed from Wind Profile-RASS Networks', *Mon. Wea. Rev.* **123**, 790–799.

Geiger, R.: 1966, *The Climate Near the Ground* (revised edition), Harvard University Press, 610 pp.

Grossman, R. L.: 1977, 'A Procedure for the Correction of Biases in Winds Measured from Aircraft', *J. Appl. Meteorol.* **6**, 654–658.

Grossman, R. L.: 1992, 'Convective Boundary Layer Budgets of Moisture and Sensible Heat over an Unstressed Prairie', *J. Geophys. Res.* **97**, 18,425–18,438.

Grossman, R. L. and Gamage, N.: 1995, 'Moisture Flux and Mixing Processes in the Daytime Continental Convective Boundary Layer', *J. Geophys. Res.* **100**, 25,665–25,674.

Hardy, K. R. and Ottersten, H.: 1969, 'Radar Investigations of Convective Patterns in the Clear Atmosphere', *J. Atmos. Sci.* **26**, 666–672.

Horst, T. W. and Oncley, S. P.: 1995, 'Flux-PAM Measurement of Scalar Fluxes Using Co-spectral Similarity', in *Proceedings Ninth Symposium on Meteorological Observations and Instrumentation*, Charlotte, INC, American Meteorological Society, pp. 495–500.

LeMone, M. A. and Grossman, R.: 2000, 'Mesoscale and Diurnal Variability of 2-m Temperature and Mixing Ratio in CASES-97', in *Proceedings of the 14th Symposium on Boundary Layer and Turbulence*, Aspen, 7–11 August, pp. 5–8.

LeMone, M. A., Grossman, R., Coulter, R., Wesely, M., Klazura, G., Poulos, G., Blumen, W., Lundquist, J., Cuenca, R., Kelly, S., Brandes, E., Oncley, S., McMillen, R., and Hicks, B.: 2000, 'Land-Atmosphere Interaction Research and Opportunities in the Walnut River Watershed in Southeast Kansas: CASES and ABLE', *Bull. Amer. Meteorol. Soc.* **81**, 757–780.

LeMone, M. A., Zhou, M., Moeng, C.-H., Lenschow, D. H., Miller, L. J., and Grossman, R. L.: 1999, 'An Observational Study of Wind Profiles in the Baroclinic Convective Planetary Boundary Layer', *Boundary-Layer Meteorol.* **90**, 47–82.

Lenschow, D. H.: 1972: *The Measurement of Air Velocity and Temperature Using the NCAR Buffalo Aircraft Measuring System*, NCAR Technical Note NCAR-TN-EDD-74, 39 pp.

Lenschow, D. H.: 1995, 'Micrometeorological Techniques for Measuring Biosphere-Atmosphere Trace Gas Exchange', in Pamela Matson and Robert Harriss (eds.), *Biogenic Trace Gages: Measuring Emissions from Soil and Water*, Chap. 5, Blackwell Science, Cambridge, MA, pp. 126–163.

Lenschow, D. H. and Stankov, B. B.: 1986, 'Length Scales in the Convective Boundary Layer', *J. Atmos. Sci.* **43**, 1198–1209.

Lenschow, D. H., Wyngaard, J. C., and Pennell, W. T.: 1980, 'Mean-Field and Second-Moment Budgets in a Baroclinic, Convective Boundary Layer', *J. Atmos. Sci.* **37**, 1313–1326.

Lilly, D. K.: 1983, 'Mesoscale Variability of the Atmosphere', *NATO Advanced Study Institute on Mesoscale Meteorology – Theories, Observations and Models*, Bonas, France, July 13–31, 1982. NATO ASI Series, Series C: Mathematical and Physical Science, **114**, 13–24.

Mahrt, L.: 1998, 'Flux Sampling Errors for Aircraft and Towers', *J. Atmos. Oceanic Tech.* **15**, 416–429.

Mahrt, L. and Ek, M.: 1993, 'Spatial Variability of Turbulent Fluxes and Roughness Lengths in HAPEX-MOBILHY', *Boundary-Layer Meteorol.* **65**, 381–400.

Mahrt, L., Sun, J., Vickers, D., MacPherson, J. I., Pederson, J. R., and Desjardins, R. L.: 1994, 'Observations of Fluxes and Inland Breezes over a Heterogeneous Surface', *J. Atmos. Sci.* **51**, 2484–2499.

Mann, J., and Lenschow, D. H.: 1994, 'Errors in Airborne Flux Measurements', *J. Geophys. Res.* **99**, 14,519–14,526.

Martner, B. E., Wuertz, D. B., Stankov, B. B., Strauch, R. G., Westwater, E. R., Gage, K. S., Ecklund, W. L., Martin, C. L., and Dabberdt, W. F.: 1993, 'An Evaluation of Wind Profiler, RASS, and Microwave Radiometer Performance', *Bull. Amer. Meteorol. Soc.* **74**, 599–613.

Millitzer, J. M., Mihaelis, M. C., Semmer, S. R., Norris, K. S., Horst, T. W., Oncley, S. P., Delany, A. C., and Brock, F. V.: 1995, 'Development of the Prototype PAM III/Flux-PAM Surface Meteorological Station', in *Proceedings Ninth Symposium on Meteorological Observations and Instrumentation*, Charlotte, NC, American Meteorological Society, pp. 490–494.

NAPAP (National Acid Precipitation Program): 1990, *Visibility: Existing and Historical Conditions – Causes and Effects*, Vol. III, Report 24, U.S. Government Printing Office, Washington, D.C., 129 pp.

Nicholls, S., LeMone, M. A., and Sommeria, G.: 1982, 'The Simulation of a Fair Weather Marine Boundary Layer in GATE Using a Three-Dimensional Model', *Quart. J. Roy. Meteorol. Soc.* **108**, 167–190.

Ou, S. C., Liou, K. N., Takano, Y., Rao, N. X., Fu, Q., Heymsfield, A. J., Miloshevich, L. M., Baum, B., and Kinne, S. A.: 1995, 'Remote Sounding of Cirrus Cloud Optical Depths and Ice Crystal Sizes from AVHRR Data: Verification Using FIRE II IFO Measurements', *J. Atmos. Sci.* **52**, 4143–4158.

Parsons, D. B., Yoneyama, K., and Redelsperger, J.-L.: 2000, 'The Evolution of the Tropical Western Pacific Atmosphere-Ocean System Following the Arrival of a Dry Intrusion', *Quart. J. Roy. Meteorol. Soc.* **126**, 517–548.

Rogers, E., Black, T. L., Deaven, D. G., DiMego, G. J., Zhao, Q., Baldwin, M., Junker, N. W., and Lin, Y.: 1996, 'Changes to the Operational "Early" Eta Analysis/Forecast System at the National Centers for Environmental Prediction', *Wea. Forecast.* **11**, 391–413.

Satheesh, S. K., and Ramanathan, V., 2000, 'Large Differences in Tropical Aerosol Forcing at the Top of the Atmosphere and Earth's Surface', *Nature* **405**, 60–63.

Segal, M., Schreiber, W. E., Kallos, G., Garratt, J. R., Rodi, A., Weaver, J., and Pielke, R. A.: 1989, 'The Impact of Crop Areas in Northeast Colorado on Midsummer Mesoscale Thermal Circulations', *Mon. Wea. Rev.* **117**, 809–825.

Sellers, P. J., Hall, F. G., Asrar, G., Strebel D. E., and Murphy, R. E.: 1992, 'An Overview of the First International Satellite Land Surface Climatology Project (ISLSCP) Field Experiment (FIFE)', *J. Geophys. Res.* **97**, 18,345–18,373.

Sellers, P. J., Margolis, H., Kelly, B., Baldocchi, D., den Hartog, J., Cihlar, J., Ryan, Goodison, B., Crill, P., Ranson, J., Lettenmaier, D., and Wickland, D.: 1995, 'The Boreal Ecosystem-Atmospheric Study (BOREAS): An Overview and Early Results from the 1994 Field Year', *Bull. Amer. Meteorol. Soc.* **76**, 1,549–1,577.

Shaw, W. J. and Doran, J. C.: 2001, 'Observations of Systematic Boundary Layer Divergence Patterns and their Relationship to Land Use and Topography', *J. Climate* **14**, 1753–1764.

Stamnes, K., Tsay, S.-C., Wilcombe, W., and Jaraweera, K.: 1988, 'Numerically Stable Algorithm for Discrete-Ordinate Method Radiative Transfer in Multiple Scattering and Emitting Layered Media', *Appl. Optics* **12**, 2502–2509.

Twine, T. E., Kustas, W. P., Norman, J. M., Cook, D. R., Houser, P. R., Meyers, T. P., Preuger, J. H., Starks, P. J., and Wesely, M. L.: 2000, 'Correcting Eddy-Covariance Flux Estimates over a Grassland', *Agric. For. Meteorol.* **103**, 279–300.

Weckwerth, T. M., Wilson, J. W., and Wakimoto, R. M.: 1996, 'Thermodynamic Variability within the Convective Boundary Layer Due to Horizontal Convective Rolls', *Mon. Wea. Rev.* **124**, 769–784.

Wellman, D. L., Wilkison, W. W., Luke, W. T., McMillen, R. T., Auble, D. L., Gunter, R. L., and Watson, T. B.: 1996, *1995 Summary Report Southern Oxidants Study: Technical Support for Airborne Measurements with Chemical and Meteorological Variables*, NOAA Technical Memo, ERL ARL-217. 56 pp.

Yates, D. N., Chen, F., LeMone, M. A., Qualls, R., Oncley, S. P., Grossman, R. L., and Brandes, E. L.: 2001, 'A CASES Dataset for Analyzing and Parameterizing the Effects of Land-Surface Heterogeneity on Area-Averaged Surface Heat Fluxes', *J. Appl. Meteorol.* **40**, 921–937.

Zipser, E. J. and Johnson, R. H.: 1998, 'Systematic Errors in Radiosonde Humidities: A Global Problem?', in *Proceedings 10th Symposium on Measurements, Observations, and Instrumentation*, Phoenix, AZ, American Meteorological Society, pp. 72–73.